APPLICATION NOTE

HOLOEYE Spatial Light Modulators

HOLOEYE Pioneers in Photonic Technology

Table of contents:

1 Introduction 2

2 Spatial Light Modulator Characterization 3

2.1 Phase Calibration 3
2.2 Wavefront Compensation 6
2.3 Diffraction efficiency camera setup 8
2.4 Spatial Light Modulators for high power applications 10

3 Applications 13

3.1 Digital Holography 13
3.1.1 Publications and References 13

3.2 Microscopy 22
3.2.1 Publications and References 22

3.3 Wavefront correction and processing 29
3.3.1 Publications and References 29

3.4 Holographic Optical Tweezer 33
3.4.1 Publications and References 33

3.5 Beam shaping with structured light 37
3.5.1 Publications and References 37

3.6 Higher Order Generation 42
3.6.1 Publications and References 42

3.7 Material Processing 50
3.7.1 Publications and References 50

3.8 Wavelength Selective Switching and Telecommunication 53
3.8.1 Publications and References 53

3.9 Mask-less and holography lithography 56
3.9.1 Publications and References 56

3.10 Polarization Generation 60
3.10.1 Publications and References 60

1 Introduction

With more than 20 years of experience in the development of spatial light modulators (SLM) and the cooperation with our partners, HOLOEYE offers products that are used world-wide in many different types of industrial and R&D applications. We are constantly working on the enhancement of our technology and look for possibilities to enable or adapt to new applications where HOLOEYE products can play a significant role.

HOLOEYE SLMs are based on 2D reflective liquid crystal on silicon (LCoS) displays with standard video resolutions. The optical and electrical anisotropy of the used LC material allows for us to modulate the phase or polarization in space and time, depending on the incident polarization orientation and applied voltage across the LC cell. Those properties make the SLM a powerful tool for various applications in the field of adaptive optics.

In this document, we will focus on our reflective phase only SLM devices. The first part includes a short overview about the most relevant SLM parameters and how they are determined at HOLOEYE. The 2nd part will focus on applications.

Figure 1: HOLOEYE Spatial Light Modulator product range

2 Spatial Light Modulator Characterization

This chapter deals with the main parameters for a phase only SLM including: phase modulation depth, stability, wave front quality, diffraction efficiency and tolerance to high power/energy illumination. We will provide a short overview about measurement principles, setups, and calibration processes for the most efficient usage.

2.1 Phase Calibration

HOLOEYE SLM products are suitable for different wavelength ranges and applications. Differences are within anti reflection and dielectric mirror coatings, and LC cell thickness for adapted phase retardation depth as well as used LC materials. An exact knowledge of the phase modulation characteristics is essential to be able to generate phase calibration curves for defined modulation requirements.

To measure the phase modulation characteristics of our reflective phase only SLMs, we use a common path interferometer (Fig 1) in combination with a fast 1D camera that can detect sub frame phase modulation with a frequency of 20 kHz. This fast time resolved phase measurement is essential since all HOLOEYE devices use fast full digital addressing.

The digital addressing also assures high reliability and a compact driver unit as basically only two voltages need to be generated. Full digital addressing leads to slight phase flicker effects that need to be investigated in order to design an optimal LC cell architecture and driving sequences for a most stable phase response.

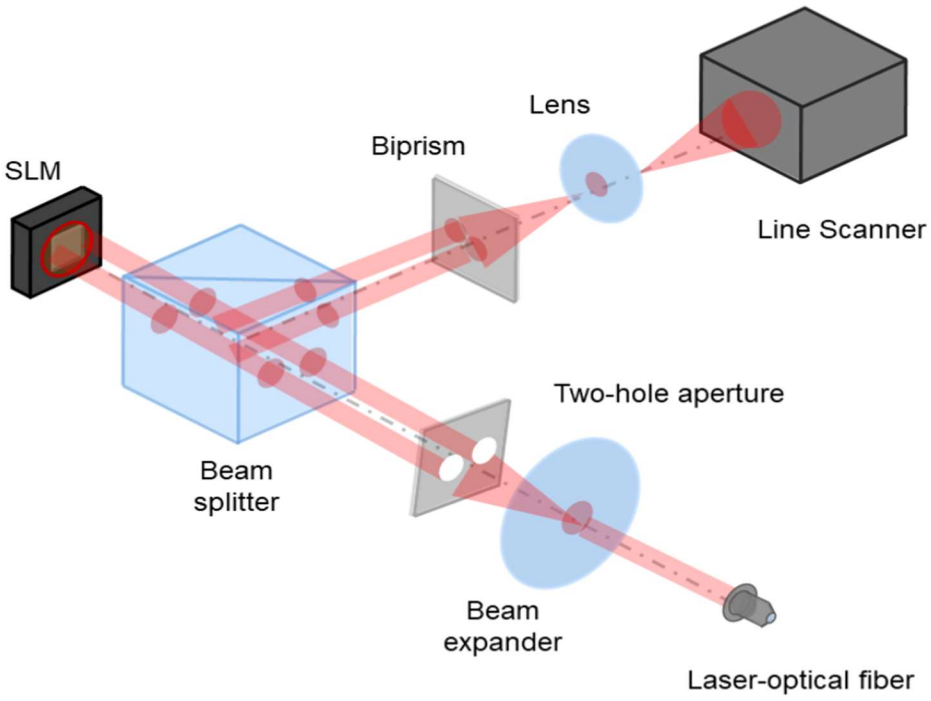

Figure 2: Optical interferometric setup for phase calibration and linearization of Spatial Light Modulators

Phase calibration and linearization of Liquid Crystal on Silicon Spatial Light Modulators is realized with interferometry setup presented in Figure 2.

The following figures show typical measurement results of the phase calibration process. On figure 2, typical phase modulation curves are presented including max phase depth (blue curve), adapted Voltage settings for ~ 2pi modulation (green curve) and the gamma corrected response for a linear 2pi phase modulation curve, which is the recommended SLM setting for most applications.
Figures 4, and 5 show the related time resolved sub frame phase response with phase flicker values for the SLM settings in figure 3.

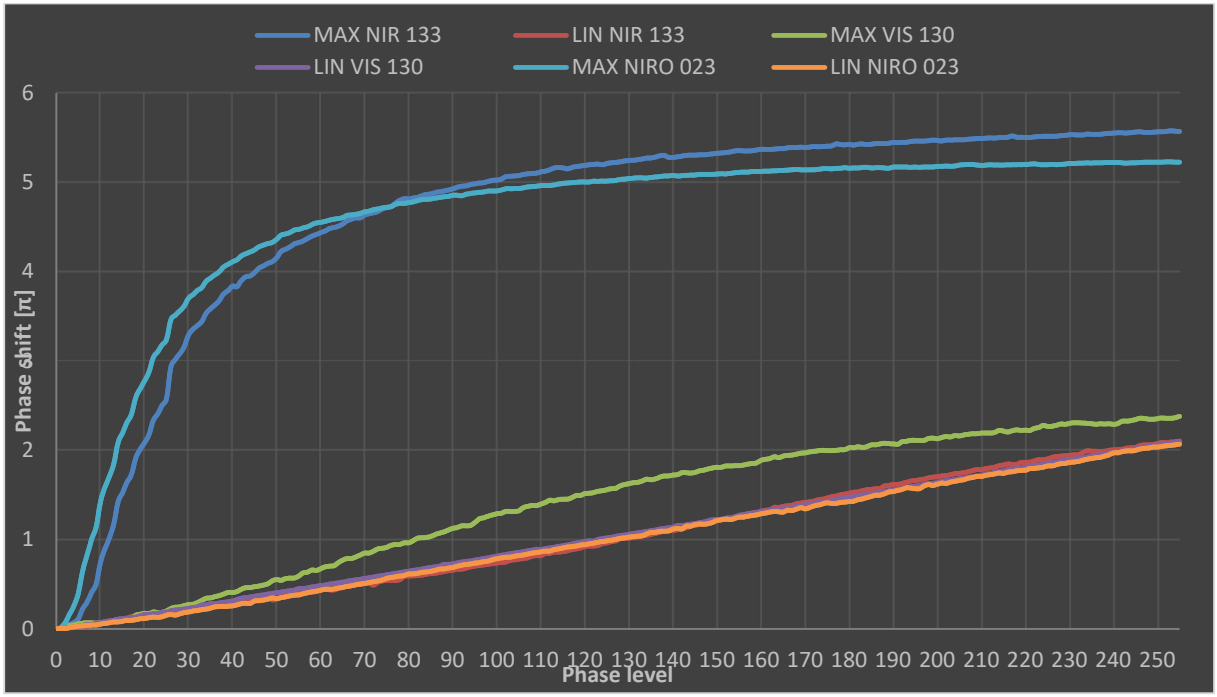

Figure 3. Phase shift calibration and final linearization measurements with PLUTO-2.1 for NIR 133, VIS 130 and NIRO 023 displays.

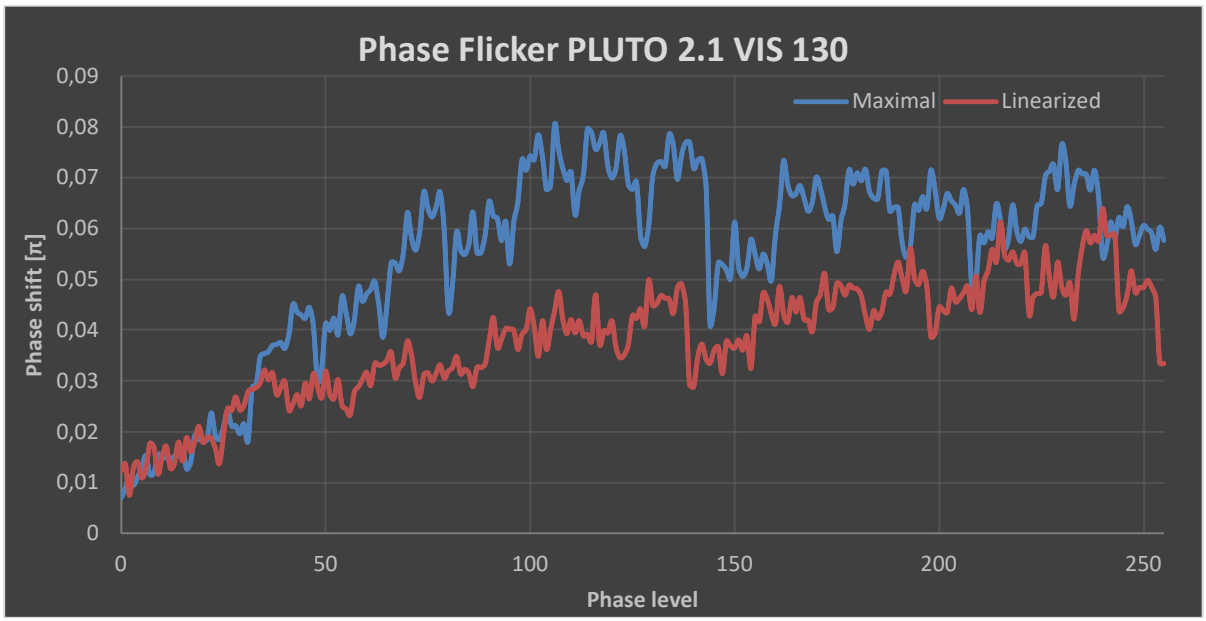

Figure 4. Phase flicker (peak to peak) calibration measurements for @520 nm with PLUTO 2.1 VIS 130

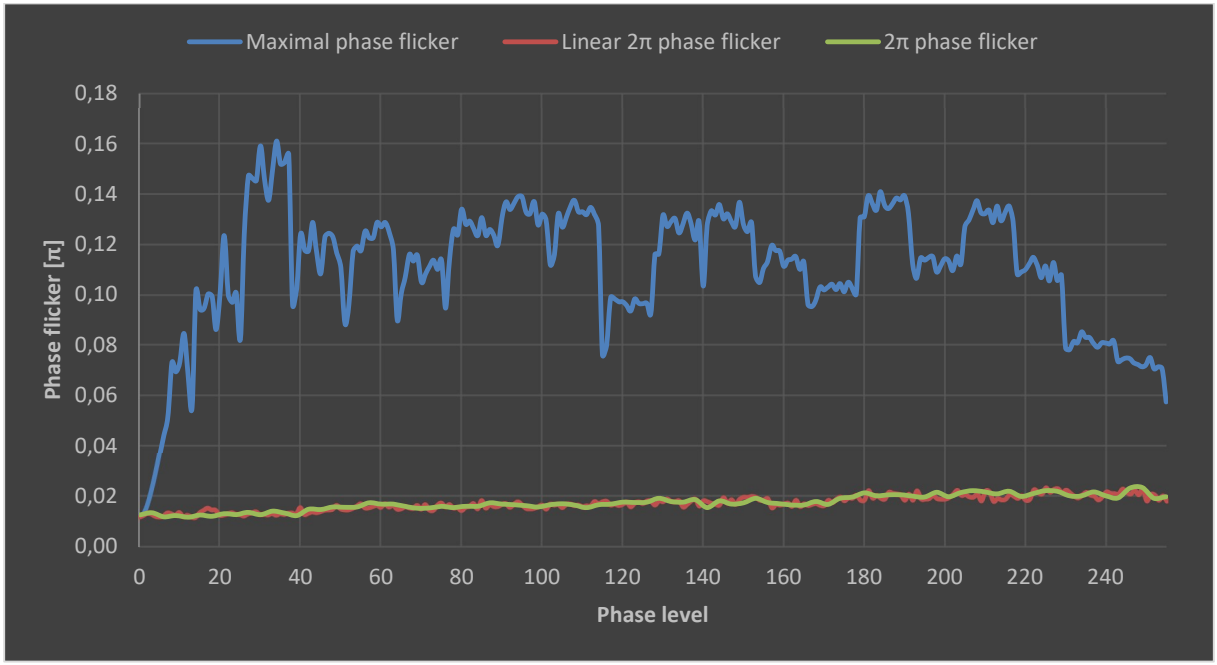

Figure 5. Phase flicker (peak to peak) calibration measurements for @1064 nm with PLUTO 2.1 NIRO 023

As one can see, the phase calibration process allows to adjust the SLM modulation characteristics for optimal performance. Linear response with desired phase shift reduces phase flicker to possible minimum values.

All presented measurements have been performed for an LCOS temperature of 30°C. Since LC viscosity is temperature dependent, temperature management provides a further degree of freedom for stabilizing the phase response. Chapter 4 includes information on an available HOLOEYE temperature management system (TMS).

2.2 Wavefront Compensation

Due to the fabrication process, the backplane of the Liquid Crystal on Silicon display is inherently not flat. This can introduce aberrations to a light beam and influence efficiency and wave front quality. Due to the nature of a 2D phase only SLM, the device is able to compensate its own flatness imperfection by addressing a compensation function. It is of great interest to characterize this wave front error and generate the corresponding compensation function.

The characterization process at HOLOEYE utilizes a Shack Hartman Sensor (SHS) and a customized Twyman-Green Interferometer (TGI). This allows for verification display deformation with two different methods, to compare data values. While the SHS setup is mainly used for a quick incoming inspection, the TGI setup is more accurate, applying a high resolution CMOS camera and a piezo steered moveable mirror for the phase shifting process.

Our TGI setup is used to generate wave front compensation functions to correct for the inherent LCoS backplane deformation as well as the ability to measure and compensate possible LC gap variations. A step-by-step description of the compensation process is presented below. Figure 6 shows the TGI setup and figure 7 shows a 3D example of reflected wave fronts before and after compensation. Figure 8 illustrates a 2D visualization (including some characterizing values) and resulting point spread functions (PSF) before and after correction.

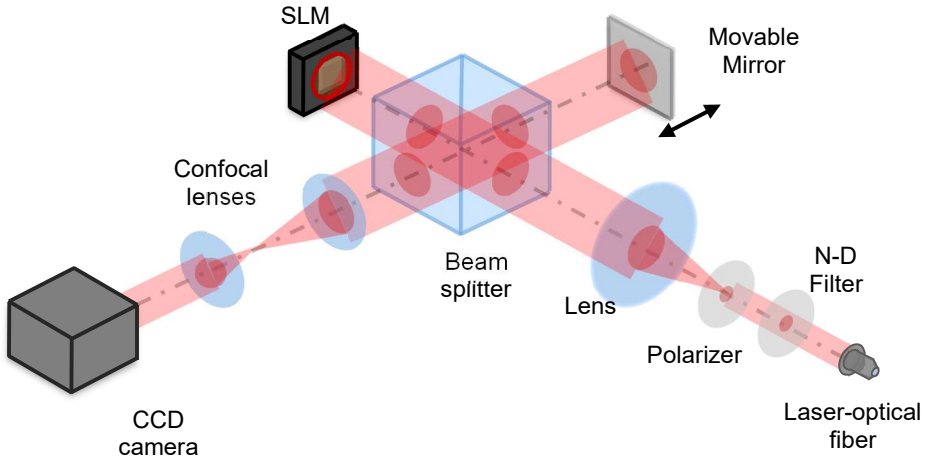

Figure 6: Optical setup for wavefront calibration based on Twyman Green interferometer.

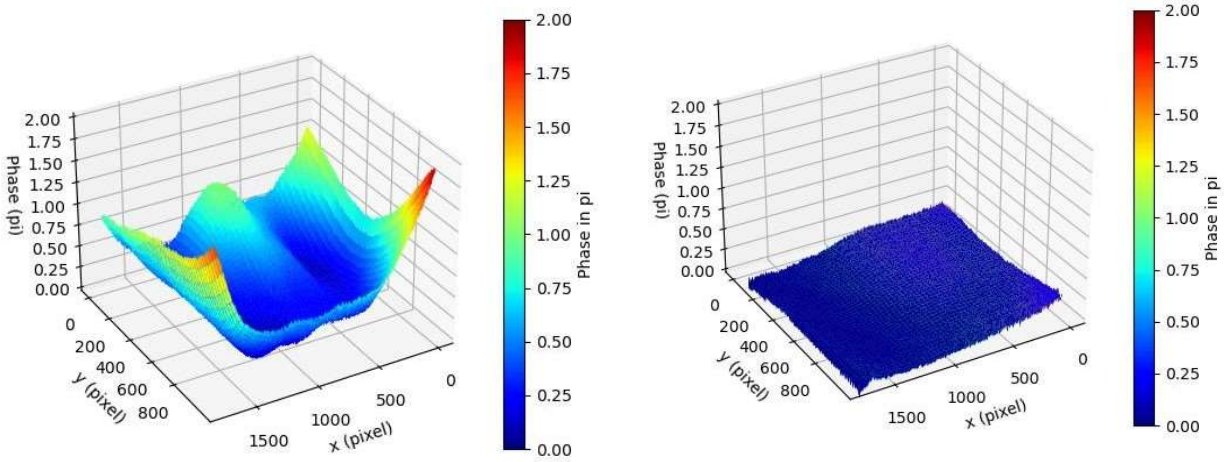

Figure 7. Measured wavefront before and after compensation for PLUTO 2.1 VIS 014. Peak Value improved from 680 nm to 103nm. RMS corrected from 108 nm to 12 nm.

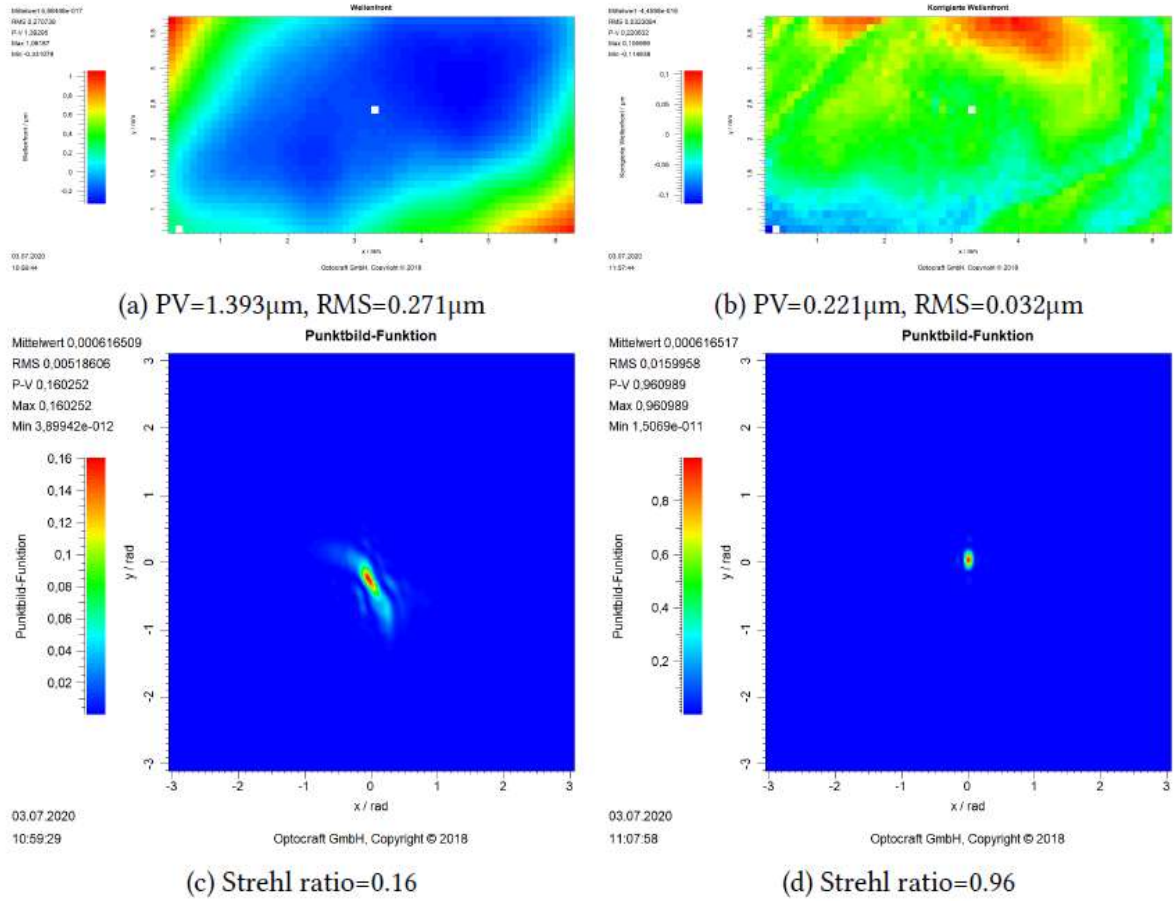

Figure 8: Wavefront and Point Spread Function measured with SHS before (a, c) and after (b, d) compensation Presented data for PLUTO 2.1 VIS 014.

An example for the impact of the compensation on the wavefront and Point Spread Function can be seen in Figure 8. Since the display has a rectangular shape, we observe an elliptical shape of the corresponding PSF. The reduction of the RMS value (from λ/2 to λ/30) and the improvement of the Strehl ratio (from 0.16 to 0.96) are considerable.

Within a production run it may occur that one of displays shows an exceptional strong deformation. But even those, strong deformations can be compensated successfully, as figure 9 demonstrates.

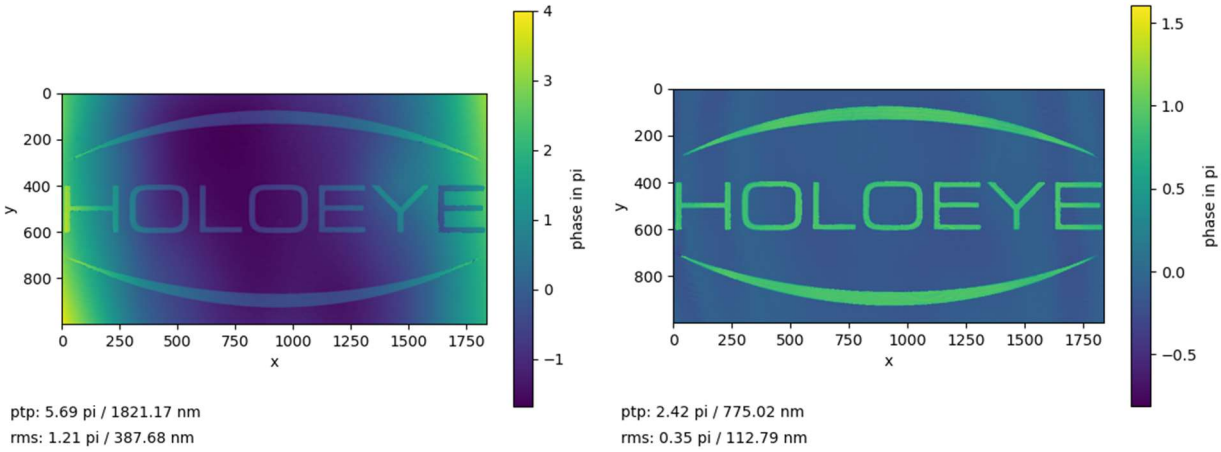

Figure 9: HOLOEYE Logo with 1π step height displayed on a spatial light modulator with strong deformation caused by production run before compensation (left) and after curvature only compensation (right).

2.3 Diffraction efficiency camera setup

2D Phase modulators can act as dynamic diffraction gratings which generates arbitrary light distributions. The simplest grating is an on-off binary (Ronchi) grating that diffracts the light in the optimal case, into a plus and a minus first diffraction order with similar intensities. The next complicated grating is a prism- or blazed grating that diffracts the light ideally in only one diffraction order. The diffraction angle depends upon the grating period and orientation, enabling a flexible beam deflection. Both simple grating versions can be used to characterize the quality of a phase only SLM and its calibration.

With an iterative Fourier algorithm, complex calculation gratings, also called computer generated holograms. (CGH) generate multiple diffraction orders which result in a 2D intensity pattern in the Fourier plane of a lens. This will be the central topic of chapter 1 in the Applications section. We will focus on the mentioned simple gratings. To measure the diffraction efficiency, we use the simple setup shown in Figure 10. The main part is a high level CCD camera with a high linearity over a wide dynamic range that is usually meant for astronomical investigations.

Results obtained with this CCD camera based setup can be a useful reference for our customers and help with quality control, the development process, and generation of optimal driving sequences and calibration data. A high degree of automation for this setup is reached by using customized software based on the HOLOEYE Software Development Kit (SDK) and provides the ability to compare different settings of our devices and optimize configurations for a wide range of wavelengths.

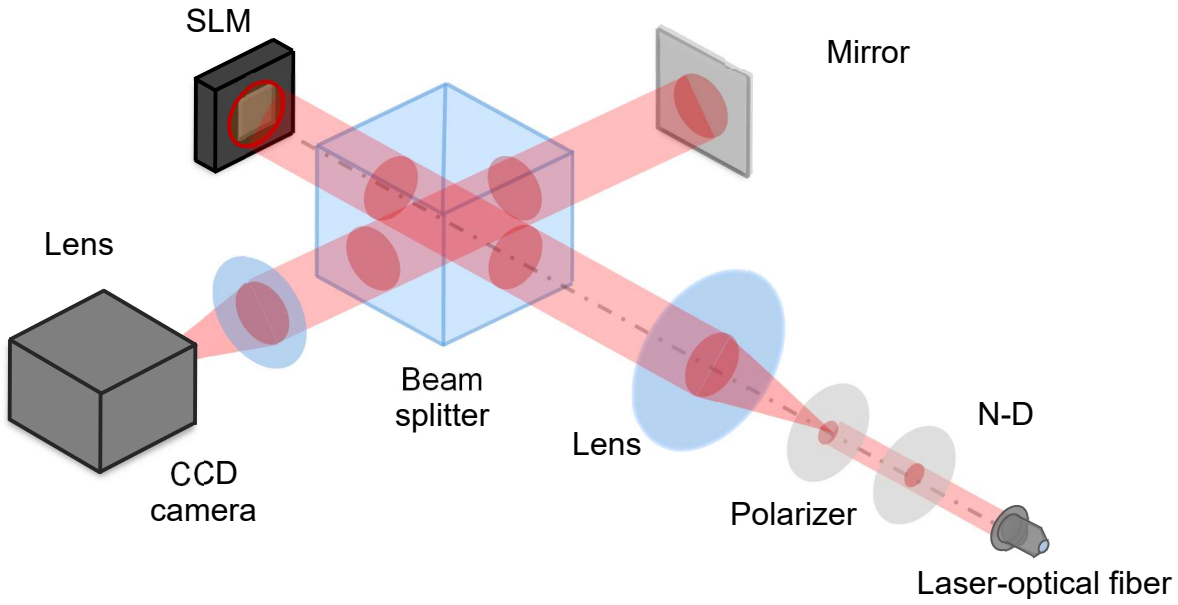

Figure 10: Diffraction efficiency setup based on a CCD camera.

Values presented in Figure 11 have been determined for 4, 8, 16 and 32 level blazed gratings at 450nm, 520nm, 637nm, 800nm, 1060nm, 1300nm and 1550nm with 9:5 sequence configuration and linearized phase response for PLUTO displays.

Data chosen for suitable HOLOEYE products depends upon the operating wavelength. Diffraction efficiency values in the figure below are seen at the 0^{th} order of uniform phase as a reference (100%)

Figure 11: Measured diffraction efficiencies of the 1st order of blazed gratings with different spatial frequencies for defined wavelengths.

2.4 Spatial Light Modulators for high power applications

Nowadays more and more applications require high power light sources. For a manufacturer it is a challenge to develop and to investigate suitable LCoS phase only display versions that can handle various types of high power and high energy lasers.

HOLOEYE designs special versions for high power use, which are equipped with a dielectric mirror coating on top of the pixel electrodes. This reduces absorption in the inter-pixel gap and diffraction losses, what leads to higher light efficiency. Due to less absorption, these display versions could be used with higher incident laser power compared to the standard versions. High average power above a couple of 10W/cm² can still lead to a heating of the LCoS display and coupled heat should be dissipated in order to assure long life time. HOLOEYE therefore offers Thermal Management Systems (TMS) that are designed for and tested with our devices in many laboratories around the world.

HOLOEYE SLMs designed for High Power applications are equipped with a dielectric mirror coating (DMC). The reflectivity for each display is optimized for the design wavelength range. Using a reflectance setup based on a white light source and a spectrometer we can provide precise data for a broadband spectrum. In Figure 12, one can see results for three phase only LCoS display versions with DMC optimized for high reflectivity and low absorption in different wavelength ranges

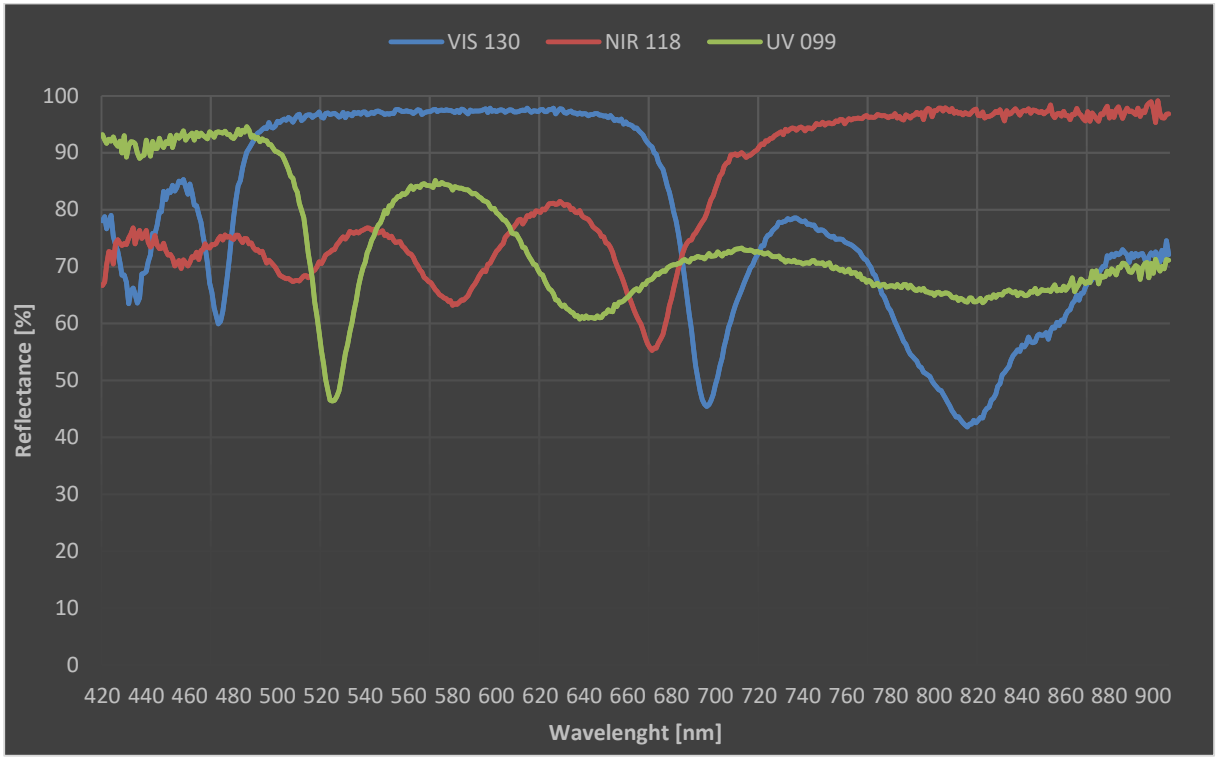

Figure 12: Wavelength dependence of the reflectance for three PLUTO-2.1 versions designed for specific wavelength ranges.

Besides reduced absorption it is of course essential to investigate the compatibility to high power and high energy light sources experimentally, what will be discussed in the following chapter.

Laser-induced damage (LID) is defined as any permanent laser radiation induced change in the characteristics of the surface/bulk of the specimen which can be observed by an inspection technique and at a sensitivity related to the intended operation of the product. Laser-induced damage threshold (LIDT) is defined as the highest quantity of laser radiation incident upon the optical component for which the extrapolated probability of damage is zero.

LID of the sample is investigated by performing a standardized S-on-1 test procedure. A LIDT value is determined by taking the average of the highest fluence value before no damage was observed and the lowest fluence value at which damage was first observed.

Those standard S-on-1 tests give a good indication of maximal power levels. However, those tests are usually done and useable for passive optical components and characteristic material damage can be determined. But absorption within the LC layer can lead to a change of characteristics before a visual physical damage occurs.

Such effects are usually also accumulative and irreversible damage can happen at lower powers after a certain time of irradiation. It is therefore of great importance to investigate the SLM characteristics while illuminating with high power / energy levels during operation to determine maximal power levels for long time exposure.

In this context it is important to us to check how our products perform under “real-life conditions”, by investigating the threshold upon which the functionality is still given. In the case of a LC-SLM we define the breakdown by a significant drop of diffraction efficiency (change of more than 10%).

Table 1 contains a collection of recent data for power handling capability, which was collected by our engineers and our customers during experiments done in high power laser laboratories.

Display	Wavelength (nm)	Pulse Width	Rep.rate (kHz)	Irradiation Time	Irradiance (W/cm2)	Fluence (mJ/cm2)	Comment
UV-099	355	15ps	250	20min/2min	6,7/10	0,027/0,04	No change / P<90%
UV-099	405	-	-	15h	8,0	-	No change
VIS-130	445	-	-	6h/2,5h	53/100	-	No change / P<90%
VIS-130	532	7,8ps	400	50min	302	0,75	P<90%
VIS-016	515	220fs	610	4h	7,00	0,012	P<90%
NIR-113	800	110fs	5	2h	15	3	P<90%
NIR-118	800	110fs	5	8h/15min	8/13,6	1,5/3	No change / P<90%
NIR-015	1030	220fs	100	60min	212/240	2,1/2,4	No change / P<90%
NIR-149	1030	10ps	50	8h	127	2,5	No change
NIR-149	1064	8,4ps	400	8h	565	1,41	No change

Table 1: Power handling capability collected with high power pulsed lasers.

HOLOEYEs Thermal Management System (TMS) improves power handling for DMC versions and for our standard panels without DMC. HOLOEYE offers two versions of Thermal Management Systems.

TMS01 is based on a Peltier element in combination with a passive heat sink.

TMS02 is prepared to work with higher laser power and is based on active water cooling. It can increase power handling of HOLOEYE devices to hundreds of Watts per cm² (cw) at around 1064 nm.

Figure 13: Display mounts compatible with Thermal Management Systems

HOLOEYE LCOS SLM displays have an integrated temperature sensor. This signal can be used for a feedback loop with the TMS through HOLOEYE configuration manager software in order to stabilize the temperature to defined values.

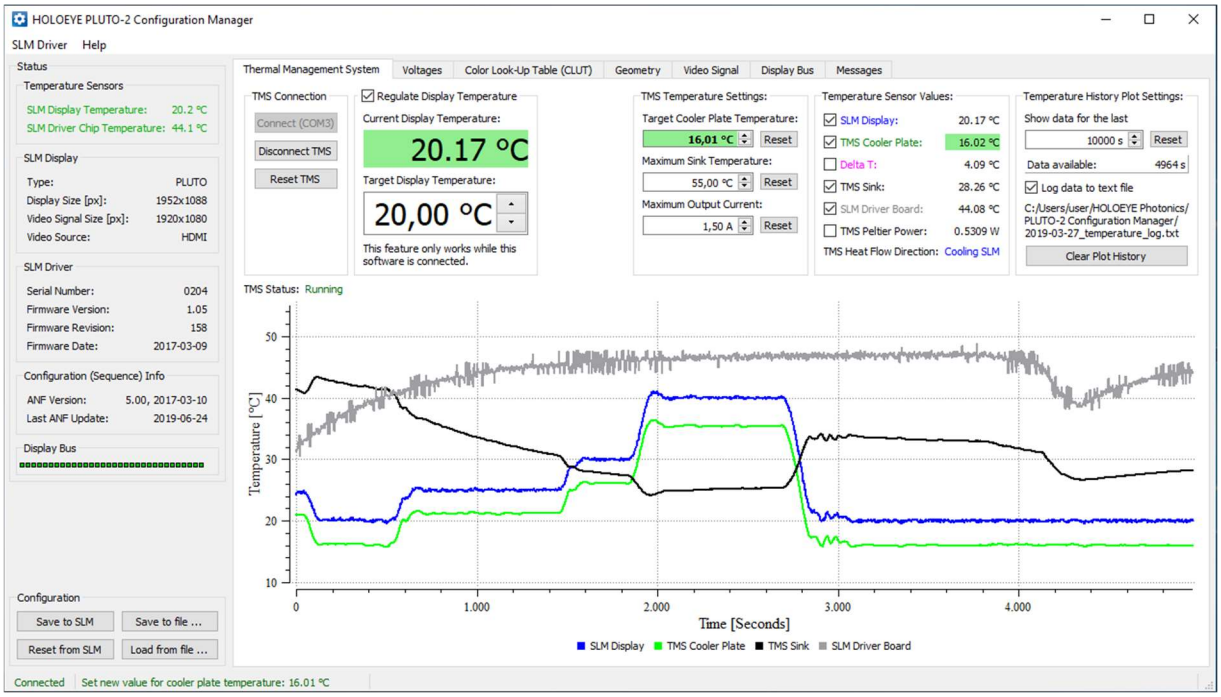

Figure 14: Screen shot of temperature stabilization using the HOLOEYE Configuration Manager software. The temperature is monitored for ~5000s and shown in a diagram. In this time the display temperature was set to multiple values (20°C, 25°C, 30°C, 40°C and back to 20°C).

3 Applications

Liquid Crystal based spatial light modulators can be used for a wide variety of different applications in the field of optics. At this document we concentrate on the most common applications.

At the end of the document, you will find an extended list of applications and HOLOEYE will be happy to send related information on request. Please also check our publication data base on our web page https://holoeye.com/category/spatial_light_modulators/

3.1 Digital Holography

Digital holography (DH) is the logical advancement of holography with respect to the availability of high resolution digital image sensors and fast signal transformations. It also permits a totally new approach for coherent optical metrology that can be described by the principle of direct numerical wavefront reconstruction. In contrast to all indirect methods that are based on the evaluation of intensity distributions, DH allows direct access to the phase of the wavefront.

Spatial light modulators give an opportunity to display digital holograms and optimize them digitally for optimal results. On presented examples you can find how SLMs were implemented into optical setups or prototypes. Experimental results underline the high quality in reconstruction and projection that could be achieved.

Industry applications: Augmented and virtual reality, metrology, quantum holography, Holographic- and Head-Up Displays.

3.1.1 Publications and References

1 Optimizing image quality for holographic near-eye displays with Michelson Holography

Suyeon Choi, Jonghyun Kim, Yifan Peng, and Gordon Wetzstein
Optica Vol. 8, Issue 2, pp. 143-146 (2021) - https://doi.org/10.1364/OPTICA.410622

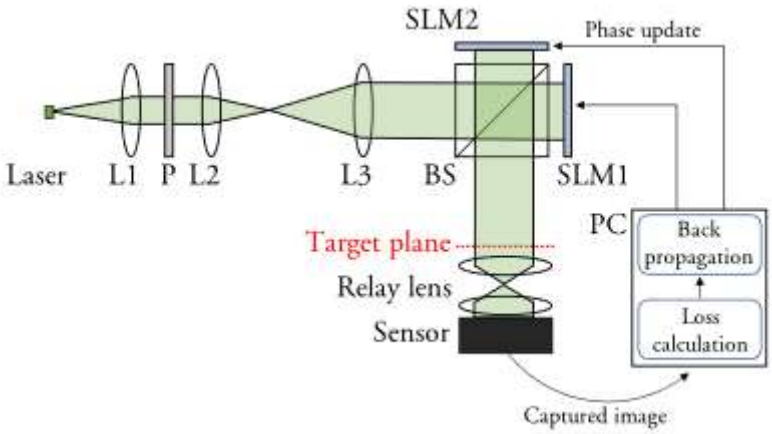

Figure 15: Principle of Michelson holography. L1: collimating lens. L2, L3: beam expander. P: polarizer. BS: beam splitter. The sensor captures the intensity of the field at the target plane. The error between captured and target images is back propagated, with a stochastic gradient descent optimization algorithm, to update the phase patterns of both SLMs.

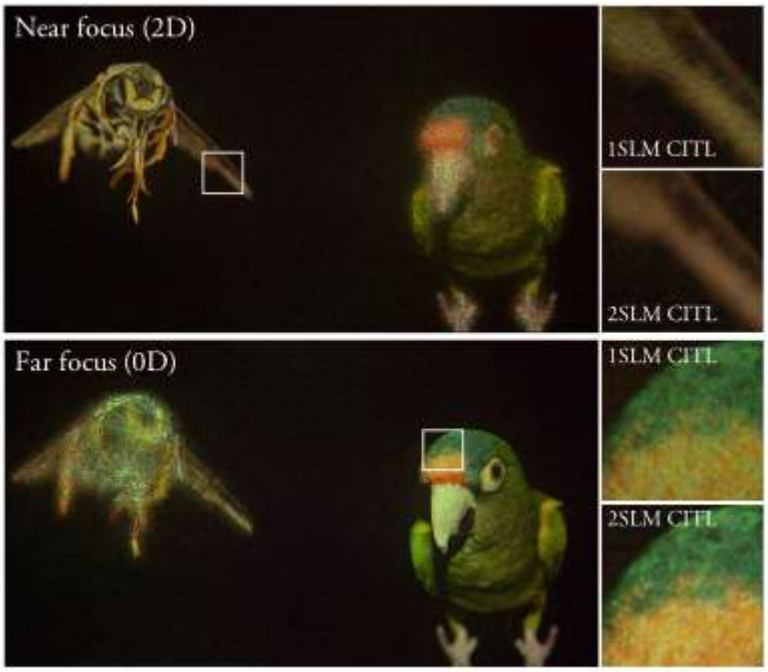

Figure 16: Experimental 3D results. The insect and the bird are located at a near (2D) and a far plane (0D), respectively. Michelson holography achieves better image quality compared to single SLM setup.

Above images courtesy of Suyeon Choi, Jonghyun Kim, Yifan Peng, Gordon Wetzstein. „Optimizing image quality for holographic near-eye displays with Michelson Holography“ (2021)

2 Holographic Near-Eye Displays for Virtual and Augmented Reality

Andrew Maimone, Andreas Georgiou and Joel S. Kollin.
ACM Transactions on Graphics, July 2017, Article No.: 85,
https://doi.org/10.1145/3072959.3073624

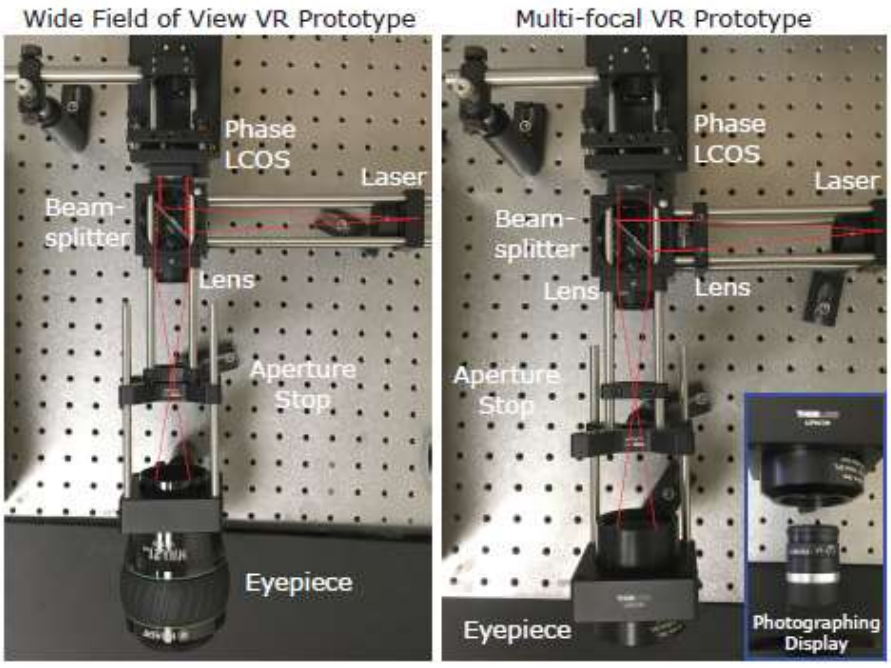

Figure 17: Virtual reality holographic display prototypes.
Left: Prototype display designed to demonstrate a wide field of view.
Right: Display designed to demonstrate multi-focal capabilities.
The blue bordered inset image shows how the display was photographed using a camera at the eye positio

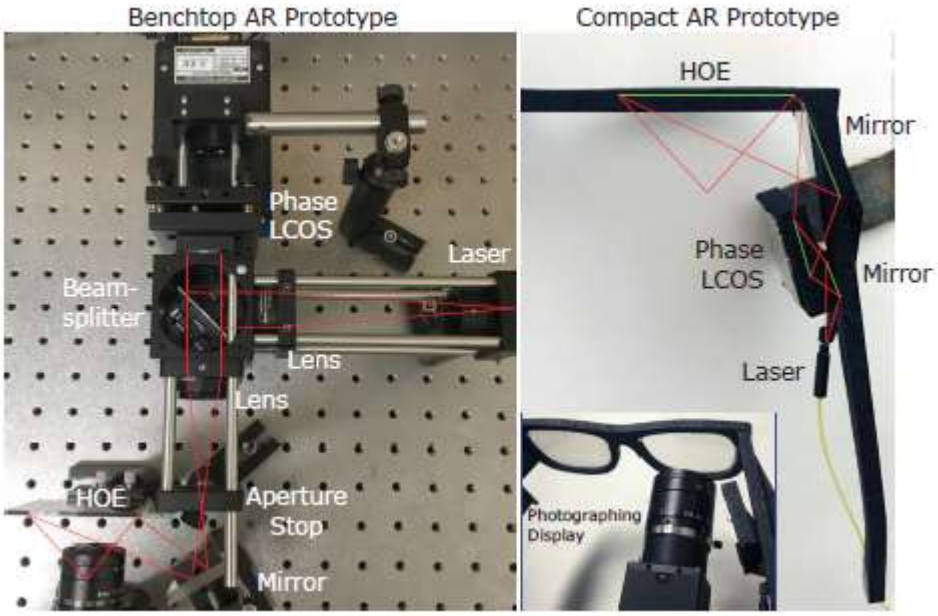

Figure 18: AR prototypes.
Left: Full color benchtop prototype.
Right: Compact prototype with miniaturized projector.
The blue border inset image shows how the display was photographed

Above images courtesy of Andrew Maimone, Andreas Georgiou and Joel S. Kollin. „Holographic Near-Eye Displays for Virtual and Augmented Reality“ (2017)

3 Wirtinger Holography for Near-Eye Displays

Praneeth Chakravarthula, Yifan Peng, Joel Kollin, Henry Fuchs and Felix Heide
ACM Transactions on Graphics, November 2019, Article No.: 213
https://doi.org/10.1145/3355089.3356539

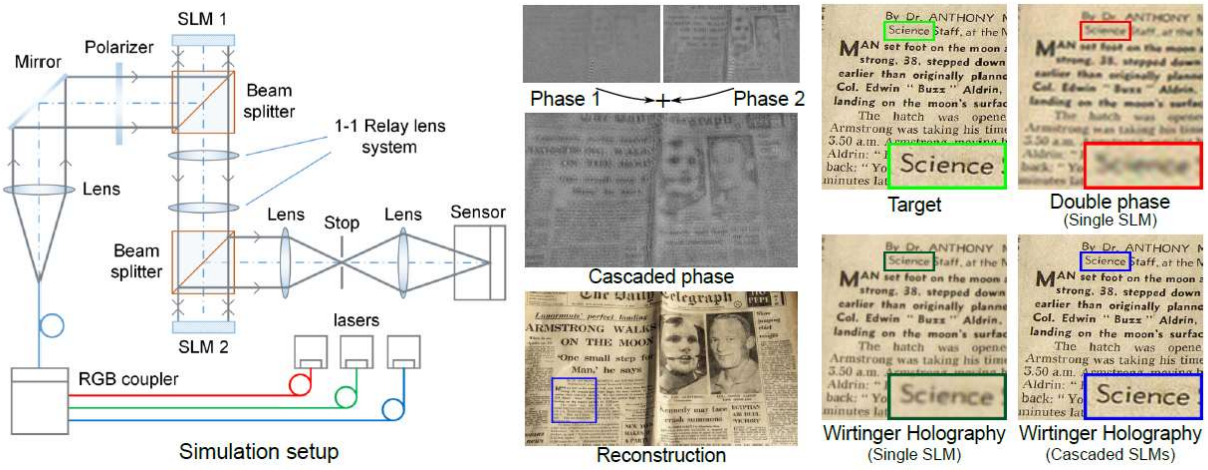

Figure 19: Schematic of setup for realizing a cascaded SLM holographic display (left), where two SLMs are relayed by optics to perform the phase modulation defined by complex matrix multiplication. The two phase holograms super-resolved a high resolution phase hologram that corresponds to reconstruct a high quality image (centre). Synthetic comparison results produced by different solutions are shown (right). Image credits Sandid/Pixabay.

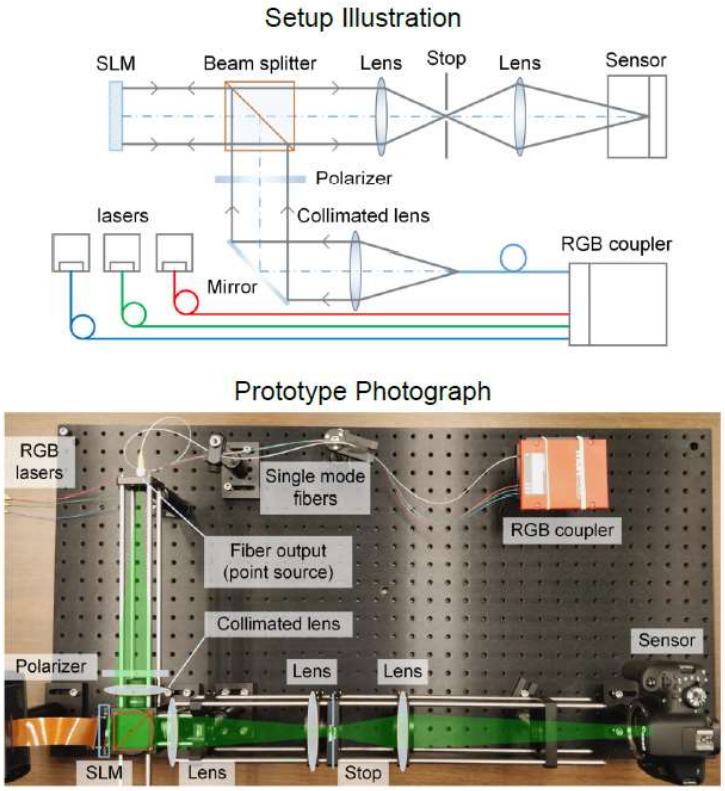

Figure 20: Schematic of our prototype holographic near-eye-display. We couple lasers of three different wavelengths into a single-mode fibre whose output end can be treated as a point source. The light emitted from the single-mode fibre is polarized and collimated before incident on the phase-only reflective Spatial Light Modulator, where the holograms are displayed. The modulated wave is imaged using a camera at the eye position.

Above images courtesy of Praneeth Chakravarthula, Yifan Peng, Joel Kollin, Henry Fuchs and Felix Heide. „Wirtinger Holography for Near-Eye Displays“ (2019)

4 Polarization entanglement-enabled quantum holography

Hugo Defienne, Bienvenu Ndagano, Ashley Lyons and Daniele Faccio.
Nature Physics (2021), https://doi.org/10.1038/s41567-020-01156-1

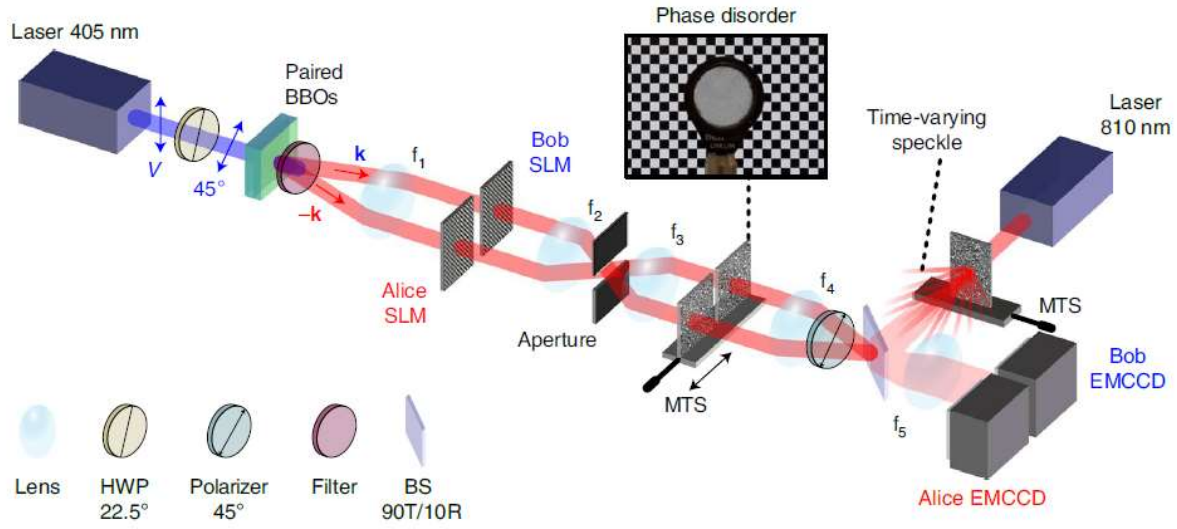

Figure 21: Experimental set-up for polarization entanglement-enabled quantum holography. Light emitted by a laser diode at 405 nm and polarized at 45° illuminates a pair of β-barium borate (BBO) crystals whose optical axes are perpendicular to each other to produce pairs of photons entangled in space and polarization by type I spontaneous parametric down-conversion. After the crystals, pump photons are filtered out by a combination of long-pass and band-pass filters. The momentum of red photons is mapped onto an SLM divided into two parts (Alice SLM and Bob SLM) by Fourier imaging with lens f1. Lenses f2-f3 image the SLM plane onto two thin diffusers (inset) positioned on a motorized translation stage (MTS) and lenses f4-f5 image it on an EMCCD camera split into two parts (Alice EMCCD and Bob EMCCD). That is, each photon of a pair experiences a phase disorder independent of that experienced by tis twin. A polarizer at 45° is positioned between lenses f4 and f5. Stray light is inserted by illuminating another dynamic diffuser with a laser (810nm) to produce a time-varying speckle pattern that is superimposed on top of quantum light using an unbalanced beam-splitter (BS 90T/10R). An adjustable aperture is positioned in the Fourier plane of the SLMs. For clarity, only two propagation paths of entangled photons at k and –k are represented, although they have a higher-dimensional spatial structure. SLMs, EMCCD cameras and diffusers are represented by pairs, although they are in practice single devices spatially divided into two independent parts. The SLM is represented in transmission, although it operates in reflection.

Above image courtesy of Hugo Defienne, Bienvenu Ndagano, Ashley Lyons and Daniele Faccio. “Polarization entanglement-enabled quantum holography” (2021)

5 Towards real time photorealistic 3D holography with deep neural networks

Liang Shi, Beichen Li, Changil Kim, Petr Kellnhofer and Wojciech Matusik
Nature volume 591, pages234–239(2021), https://doi.org/10.1038/s41586-020-03152-0

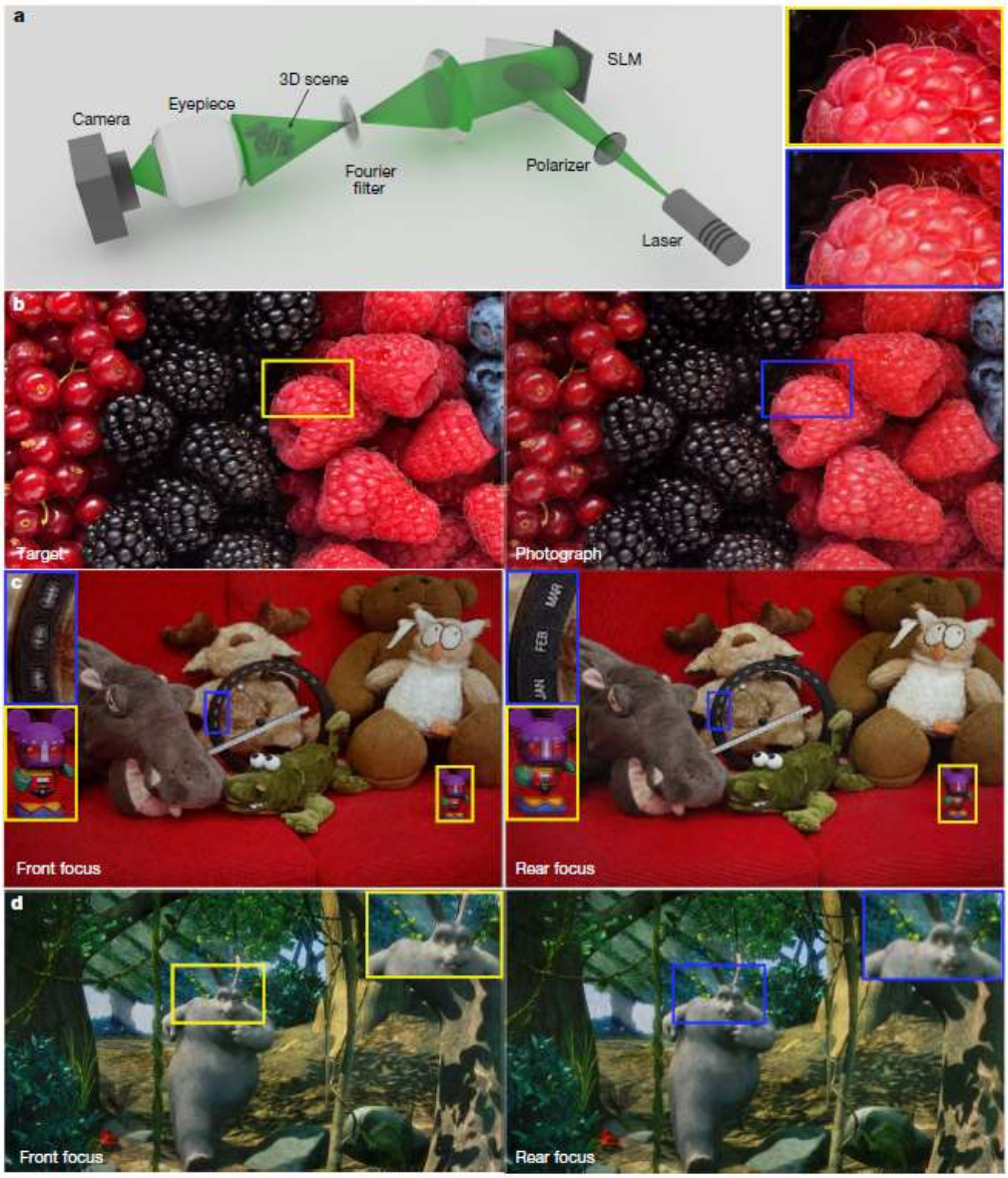

Figure 22: Experimental demonstration of 2D and 3D holographic projection.

a) Scheme of our phase-only holographic display prototype. Only the green laser is visualized.
b) Left: a flat (2D) target image for testing the spatial resolution of our prototype. Right: A photograph of the CNN predicted hologram (encoded with anti-aliasing double phase method) displayed on our prototype.
The insets on the top right show the magnified bounding boxes
c) Photographs of our prototype presenting a real-world captured 3D couch scene. The left photograph is focused on the mouse toy and the right photograph is focused on the perpetual desk calendar.
d) Photographs of our prototype presenting a computer-rendered 3D Big Buck Bunny scene. The left photograph is focused the bunny´s eye and the right photograph is focused background tree leaves.

Credit: Ana Blazic Pavlovic/shutterstock.com; image reproduced from www.bigbuckbunny.org (@2008, Blender Foundation) under a Creative Commons license (https://creativecommons.org/licenses/by/3.0/)

Above images courtesy of Liang Shi, Beichen Li, Changil Kim, Petr Kellnhofer and Wojciech Matusik “Towards real time photorealistic 3D holography with deep neural networks” (2020) http://cgh.csail.mit.edu/

6 Neural Holography with Camera-in-the-loop Training

Yifan Peng, Suyeon Choi, Nitish Padmanaban, Gordon Wetzstein
ACM Transactions on Graphics, November 2020, Article No.: 185,
https://doi.org/10.1145/3414685.3417802

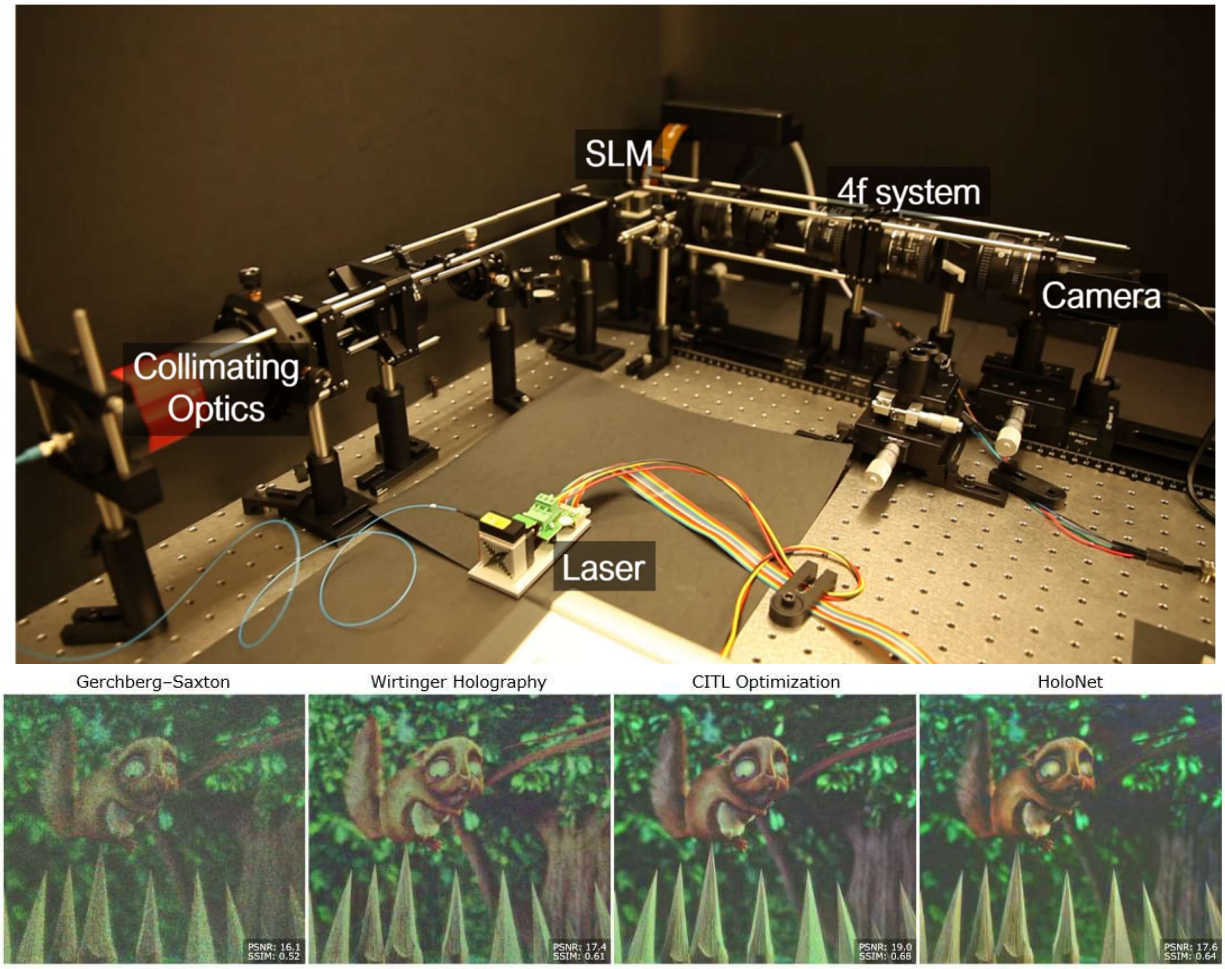

Figure 23: Above: Holographic display prototype. Our benchtop display uses a fiber-coupled RGB laser module, collimating optics, a liquid crystal on silicon (LCoS) spatial light modulator and a machine vision camera.
Bottom: Comparison of computer-generated holography (CGH) algorithms captured with a prototype holographic near-eye display. The classic Gerchberg-Saxton approach is intuitive but it suffers from speckle and other artifacts (left). Wirtinger Holography was recently introduced as an iterative CGH method that achieves better image quality (center left). We introduce camera-in-the-loop (CITL) optimization strategies that achieve unprecedented holographic image quality (center right). Moreover, we introduce a neural network architecture, HoloNet, that achieves a quality comparable to the best existing iterative approaches in real time for full-resolution 1080p images (right).

Above images courtesy of Yifan Peng, Suyeon Choi, Nitish Padmanaban, Gordon Wetzstein. "Neural Holography with Camera-in-the-loop Training", 2020

http://www.computationalimaging.org/publications/neuralholography/

7 Fourier horizontal parallax only computer and digital holography of large size

Tomasz Kozacki, Juan Martinez-Carranza, Rafal Kukolowicz, Maksymilian Chlipala
Optica, June 2021, Vol. 29, No. 12,
https://doi.org/10.1364/OE.421186

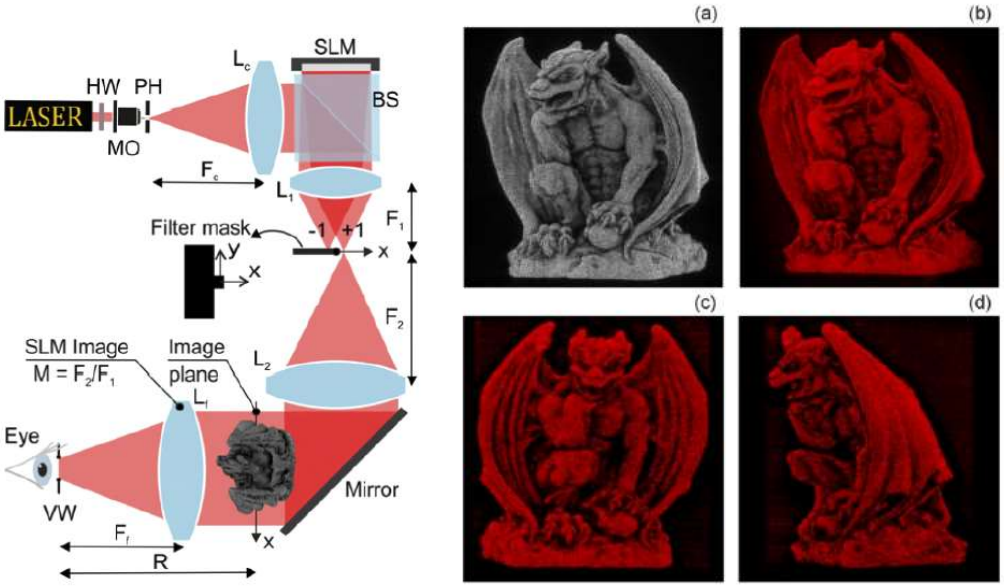

Figure 194: Left: Fourier holographic display scheme. Right: Experimental angle view (a) numerical and (b) optical reconstructions of center view (0°) and optical reconstructions of (c) left and (d) right end view (42°).

Above images courtesy of Tomasz Kozacki, Juan Martinez-Carranza, Rafał Kukołowicz, Maksymilian Chlipała
“Fourier horizontal parallax only computer and digital holography of large size”, 2021

8 Holographic near-eye display based on complex amplitude modulation with band-limited zone plates

Yun Chen, Minjie Hua, Tianshun Zhang, Mingxin Zhou, Jianhong Wu, Wenlong Zou
Optics Express, 2021, Vol. 29,Issue 14,
https://doi.org/10.1364/OE.431032

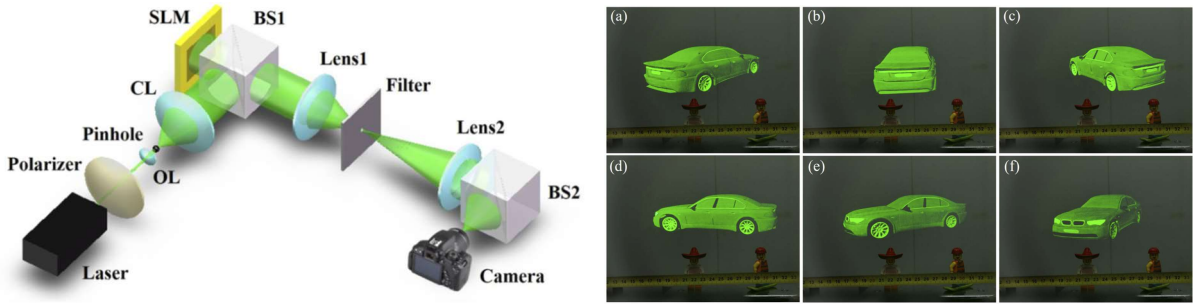

Figure 205: Left: Schematic illustration of the experimental system for the proposed holographic Near Eye Display Right: Dynamic holographic 3D AR display. (a)-(f) are the six extracted frames from the video: https://opticapublishing.figshare.com/articles/media/Visualization1_mp4/14587464

Above images courtesy of Yun Chen, Minjie Hua, Tianshun Zhang, Mingxin Zhou, Jianhong Wu, Wenlong Zu
“Holographic near-eye display based on complex amplitude modulation with band-limited zone plates”, 2021

More related publications:

9 Dynamic 2D implementation of 3D diffractive optics

Haiyan Wang, Rafael Piestun
Optica Vol. 5, Issue 10, pp. 1220-1228 (2018), https://doi.org/10.1364/OPTICA.5.001220

10 Compact design for optical-see-through holographic displays employing holographic optical elements

Pengcheng Zhou, Yan Li, Shuxin Liu, and Yikai Su
Optics Express Vol. 26, Issue 18, pp. 22866-22876 (2018)
https://doi.org/10.1364/OE.26.022866

11 Holographic near-eye display with continuously expanded eye-box using two-dimensional replication and angular spectrum wrapping

Myeong-Ho Choi, Yeon-Gyeong Ju, and Jae-Hyeung Park
Optics Express Vol. 28, Issue 1, pp. 533-547 (2020), https://doi.org/10.1364/OE.381277

12 Optical see-through holographic near-eye-display with eye-box steering and depth of field control

Jae-Hyeung Park and Seong-Bok Kim
Optics Express Vol. 26, Issue 21, pp. 27076-27088 (2018)
https://doi.org/10.1364/OE.26.027076

13 Hologram generation via Hilbert transform

Tomoyoshi Shimobaba, Takashi Kakue, Yota Yamamoto, Ikuo Hoshi, Harutaka Shiomi, Takashi Nishitsuji, Naoki Takada, and Tomoyoshi Ito
OSA Continuum Vol. 3, Issue 6, pp. 1498-1503 (2020)
https://doi.org/10.1364/OSAC.395003

14 Fabrication of oil-water separation copper filter by spatial light modulated femtosecond laser

Xiaoyan Sun, Zhuolin Dong, Kaifan Cheng, Dongkai Chu, Dejian Kong, Youwang Hu and Ji'an Duan
Journal of Micromechanics and Microengineering, Volume 30, Number 6 (2020),
https://doi.org/10.1088/1361-6439/ab870d

15 Rapid tilted-plane Gerchberg-Saxton algorithm for holographic optical tweezers

Yanan Cai, Shaohui Yan, Zhaojun Wang, Runze Li, Yansheng Liang, Yuan Zhou, Xing Li, Xianghua Yu, Ming Lei, and Baoli Yao
Optics Express Vol. 28, Issue 9, pp. 12729-12739 (2020)
https://doi.org/10.1364/OE.389897

3.2 Microscopy

Within optical setups designed for microscopy, a Spatial Light Modulator can be applied in different functions. On the one hand as a dynamic diffractive optical element in the illumination path the SLM gives the flexibility to shape and steer the light e.g. for structured illumination or light sheet microscopy.

On the other hand placed into the detection path, a variety of contrast techniques can be implemented by introducing the corresponding phase masks. Furthermore, the SLM can correct for aberration introduced by the specimen and other optical elements, including SLM itself.

Industry applications: Two-photon microscopy, laser-scanning microscopy, absorption microscopy, light sheet microscopy, phase contrast imaging

3.2.1 Publications and References

1 Observing the cell in its native state: Imaging subcellular dynamics in multicellar organisms

Tsung-Li Liu1, Srigokul Upadhyayula, Daniel E. Milkie, Ved Singh, Kai Wang, Ian A. Swinburne, Kishore R. Mosaliganti, Zach M. Collins, Tom W. Hiscock, Jamien Shea, Abraham Q. Kohrman, Taylor N. Medwig, Daphne Dambournet, Ryan Forster, Brian Cunniff, Yuan Ruan, Hanako Yashiro, Steffen Scholpp, Elliot M. Meyerowitz, Dirk Hockemeyer, David G. Drubin, Benjamin L. Martin, David Q. Matus, Minoru Koyama, Sean G. Megason, Tom Kirchhausen, Eric Betzig Science 20 Apr 2018, Vol. 360, Issue 6386, eaaq1392, DOI: 10.1126/science.aaq1392

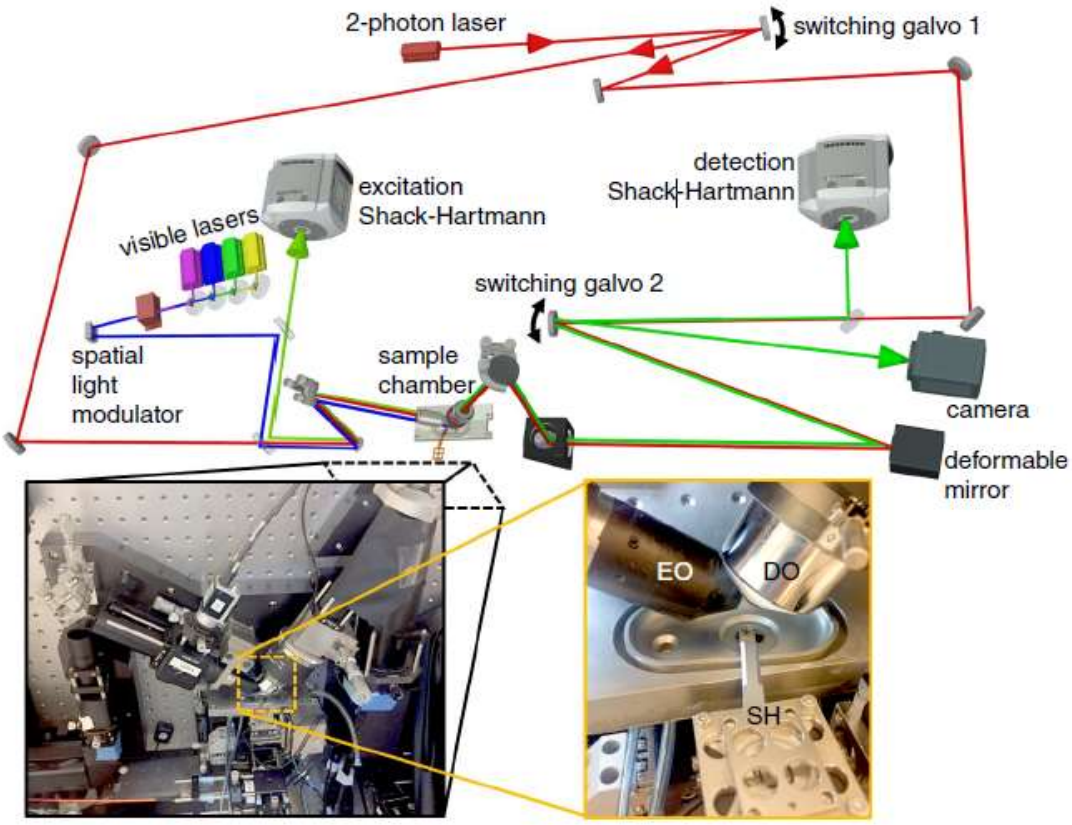

Figure 216: Simplified microscope schematic. EO: excitation objective. DO: detection objective. SH: sample holder

Above image courtesy of Tsung-Li Liu. “Observing the cell in its native state: Imaging subcellular dynamics in multicellar organisms.” (2018)

2 Far-field imaging of non-fluorescent species with subdiffraction resolution

Pu Wang, Mikhail N. Slipchenko, James Mitchell, Chen Yang, Eric O. Potma, Xianfan Xu, Ji-Xin Cheng
Nature Photon 7, 449–453 (2013). https://doi.org/10.1038/nphoton.2013.97

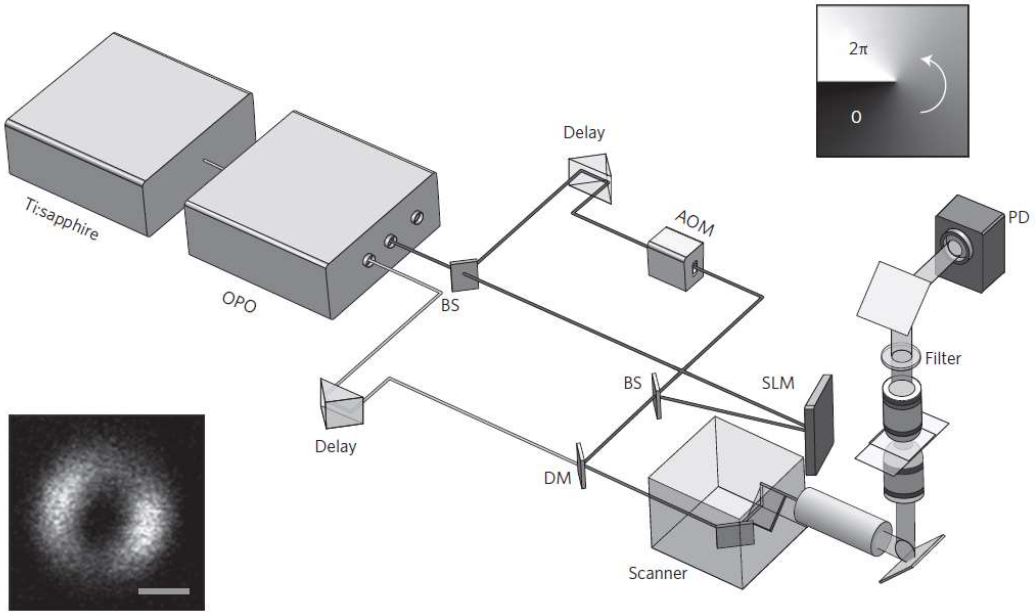

Figure 227: Diagram of the saturated transient absorption microscope. OPO: optical parametric oscillator. AOM: acousto-optic modulator. BS: beam splitter. SLM: Spatial Light Modulator. PD: Photodiode. DM: dichroic mirror.
Upper right inset: the helix phase pattern sent to the SLM to generate a doughnut-shaped focus of the saturation beam.
Lower left inset: the measured PSF of the saturation beam using second-harmonic imaging of 20 nm ZnO nanocrystals. Scale bar: 500 nm

Above image courtesy of Pu Wang, Mikhail N. Slipchenko, James Mitchell, Chen Yang Eric O. Patoma, Xianfan Xu and Ji-Xin Cheng, „Far-field imaging of non-fliorescent species with subdiffraction resolution“ (2013)

3 Single shot, three-dimensional fluorescence microscopy with a spatially rotating point spread function

Zhaojun Wang, Yanan Cai, Yansheng Liang, Xing Zhou, Shaohui Yan, Dan Dan, Piero R. Bianco, Ming Lei, and Baoli Yao
Biomedical Optics Express Vol. 8, Issue 12, pp. 5493-5506 (2017),
https://doi.org/10.1364/BOE.8.005493

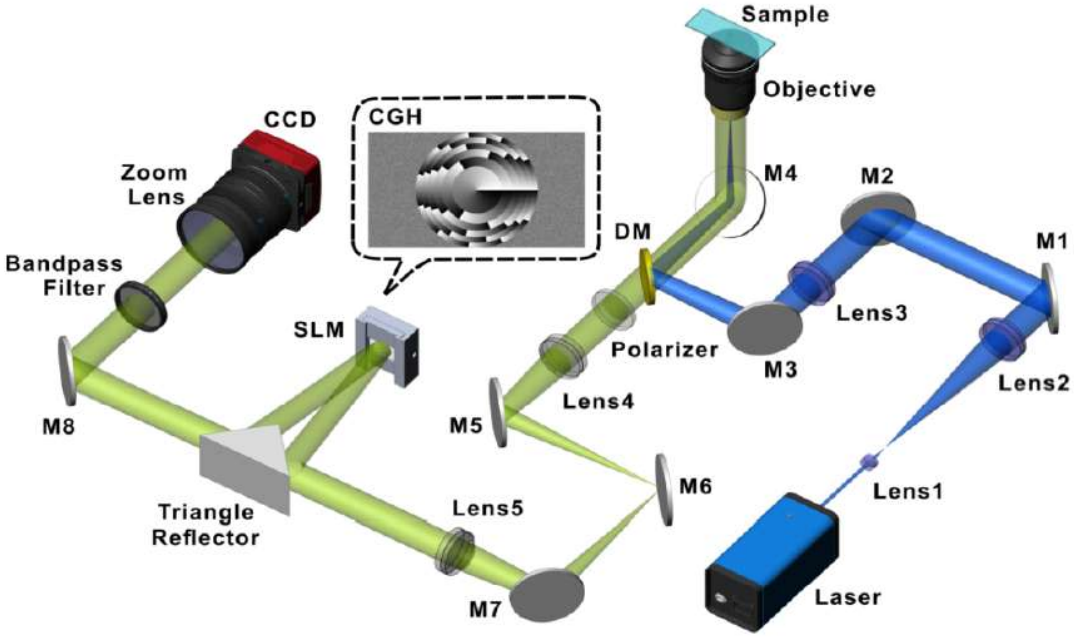

Figure 238: Schematic of the single shot, three-dimensional fluorescence microscope. The expanded and collimated beam is projected in parallel onto the specimen as an epi-illumination source. The wavefront of the fluorescence beam emitted from the specimen is modulated by the spatial light modulator, which is lasted focused onto CCD camera. The inset shows an example of the loaded CGH on the spatial light modulator. DM: long pass dichroic mirror (λ=500 nm). SLM: Spatial Light Modulator. M1-M8: mirrors.

Above image courtesy of Zhaojun Wang and Yanan Cai and Yansheng Liang and Xing Zhou and Shaohui Yan and Dan Dan and Piero R. Bianco and Ming Lei and Baoli Yao. „Single shot, three-dimensional fluorescence microscopy with a spatially rotating point spread function“ (2017)

4 Spatial Light Modulator Microscopy

Volodymyr Nikolenko, Darcy S. Peterka, Roberto Araya, Alan Woodruff, Rafael Yuste
Cold Spring Harbor Protocols – December 2013
DOI: 10.1101/pdb.top079517

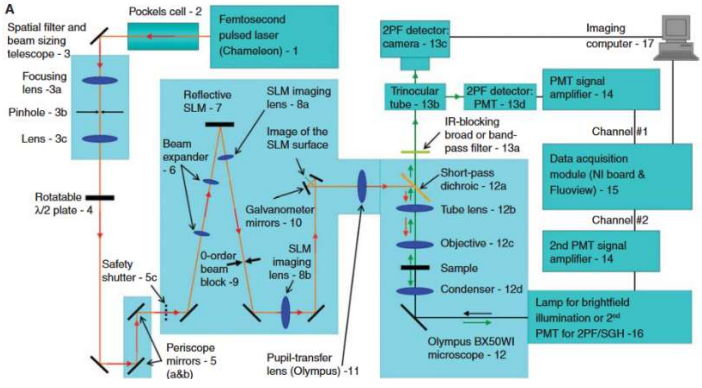

Figure 29: Optical diagram of the Spatial Light Modulator microscopy system used in laboratory.

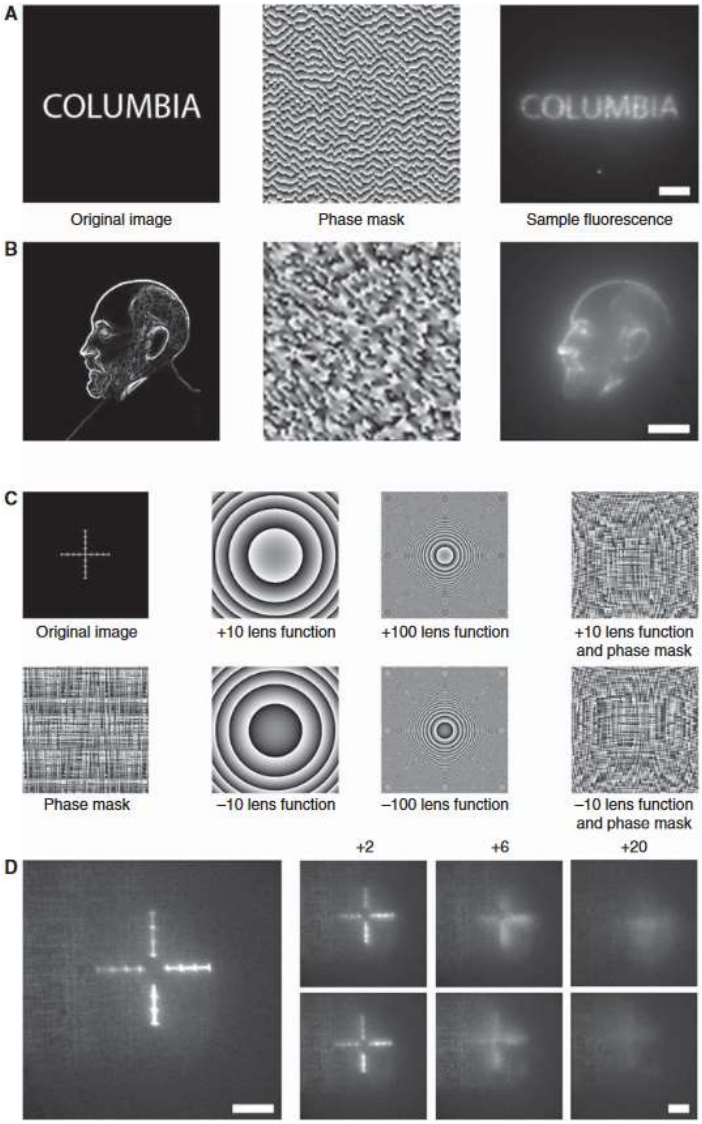

Figure 30: Spatial Light Modulator light patterning and depth focusing. Imaging samples from an agarose gel saturated with Alexa Fluor 488 fluorescence indicator to test the efficiency of two-photon excitation. Images were acquired using a 60x0.9 numerical aperture objective.

(A) A simple binary bitmap pattern was uploaded into SLM software, and the phase mask obtained is shown in the middle panel. Grayscale corresponds to a phase shift from 0 to 2π. The resulting two-photon fluorescence image of the sample acquired with the CCD is shown on the right panel. These data also show that liquid-crystal-based diffractive SLMs can withstand structured nonlinear illumination.
(B) Complex grayscale patterns can be used to program the SLM. A stylized picture of Santiago Ramon Cajal, based on a historical photograph, was used.
(C) Focusing with an SLM. The SLM software allows additional optical functions to be applied on top of the phase mask. In this example. A lens function was used to shift the focus of excitation in the axial dimension. The original image and its corresponding phase mask as well as the lens phase function alone added to the original phase mask are shown.
(D) Two-photon fluorescence image of the test pattern acquired with the CCD camera. The virtual focus plane is moved away in both directions from the camera's imagining plane using a lens function of corresponding strength

Above images courtesy of Volodymyr Nikolenko, Darcy S. Peterka, Roberto Araya, Alan Woodruff, Rafael Yuste "Spatial Light Modulator Microscopy " (2013)

5 Light-sheet microscopy with length-adaptive Bessel beams

Tobias Meinert and Alexander Rohrbach
Biomedical Optics Express Vol. 10, Issue 2, pp. 670-681 (2019), https://doi.org/10.1364/BOE.10.000670

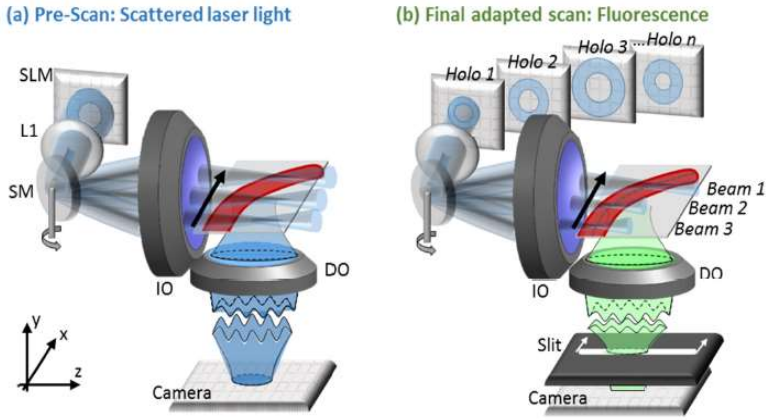

*Figure 31: Setup sketch for a light-sheet microscope using length-adapted Bessel beams. Here, a SLM is used for beam formation. The scan mirror (SM) placed in a plane conjugated to the BFP of the illumination objective (IO) scans the phase shaped beam through the focal plane of the detection objective (DO). **(a)** In a pre-scan, the shape of the object is estimated by using constant, long Bessel beams and scattered laser light images to a camera. **(b)** Different amplitude modulations of the holograms on the SLM adapt the focal positions and the beam lengths to the shape of the object (depicted in red) varying at each scan position. The DO and a tube lens (not shown) image the fluorescent light onto the camera, equipped with a rolling shutter (slit) to enable line-confocal detection.*

Above image courtesy of Tobias Meinert and Alexander Rohrbach. “Light-sheet microscopy with length-adaptive Bessel beams”, 2019, Biomedical Optics Express

6 Synchronization-free light sheet microscopy based on a 2D phase mask

Yina Chang, Chenyang Wen, Chenglin Gu, and Shih-Chi Chen
Optica Vol. 4, Issue 9, pp. 1030-1033 (2017), https://doi.org/10.1364/OPTICA.4.001030

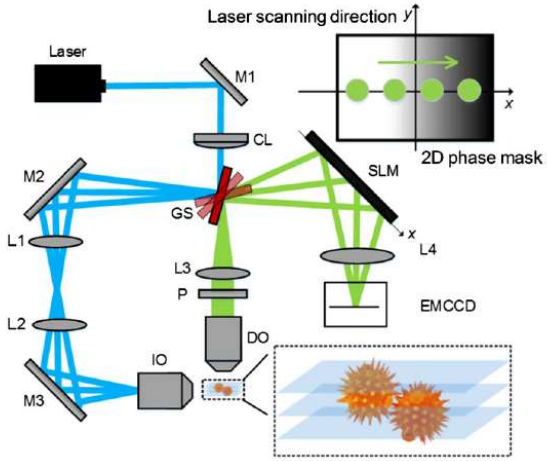

Figure 32: Optical configuration of the light sheet microscope (LSM). CL: cylindrical lens DO: detection objective GS: galvanometric scanner IO: illumination objective DO: detection objective P: polarizer EMCCD: electron multiplying charge coupled device.
It is worthwhile to note that the LC-SLM is used in the system to quickly evaluate the different phase mask designs, and during volume scanning process, the phase patterns on the LC-SLM remain unchanged.

Above image Courtesy of Yina Chang, Chenyang Wen, Chenglin Gu, Shih-Chi Chen. “Synchronization-free light sheet microscopy based on a 2D phase mask”, 2017, Optica

7 2.5D microscopy with polarization independent SLM for enhanced detection efficiency and aberration correction

Jinhan Ren, Kyu Young Han
Optics Express 27530, Vol. 29, No. 17, 16 Aug 2021

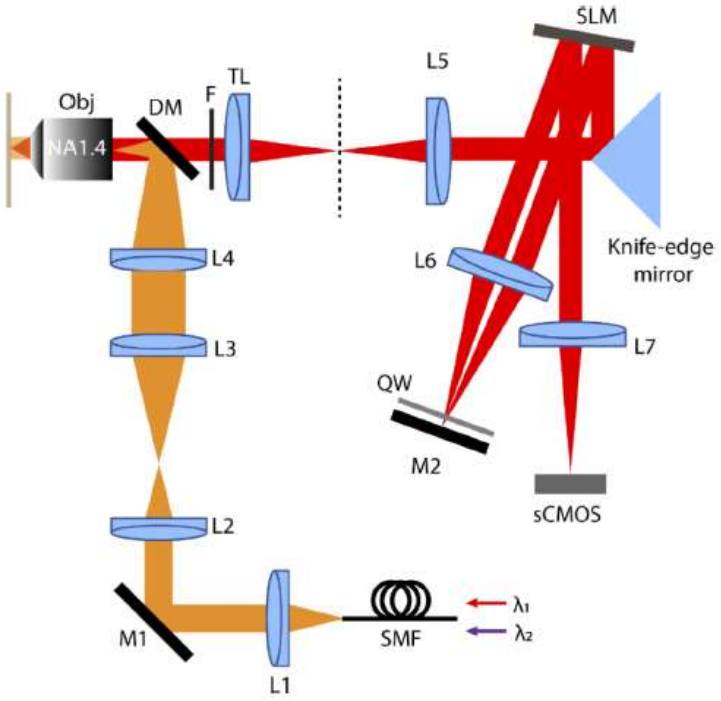

Figure 33: 2.5 D microscope with double-pass SLM configuration. λ1=638 nm, λ2= 405 nm, DM: dichroic mirrors, F: multiband emission filter, L1-7: lenses, TL: tube lens, M1-2: mirrors, OBJ. objective lens, QW: quarter waveplate, SLM: Spatial Light Modulator, SMF: single mode fiber

Above image Courtesy of Jinhan Ren, Kyu Young Han. “2.5D microscopy with polarization independent SLM for enhanced detection efficiency and aberration correction”, 2021, Optics Express

More related publications:

8 Velocity measurements with structured light transmitted through a multimode optical fiber using digital optical phase conjugation

Lars Büttner, Martin Thümmler, and Jürgen Czarske
Optics Express Vol. 28, Issue 6, pp. 8064-8075 (2020), https://doi.org/10.1364/OE.386047

9 Encoding of arbitrary micrometric complex illumination patterns with reduced speckle

Miguel Carbonell-Leal, Gladys Mínguez-Vega, Jesús Lancis, and Omel Mendoza-Yero
Optics Express Vol. 27, Issue 14, pp. 19788-19801 (2019)
https://doi.org/10.1364/OE.27.019788

10 Endogenous SHG and 2PEF coherence imaging of substructures in neurons in 3D

Carlos Macias-Romero, Claire Teulon, Marie Didier, and Sylvie Roke
Optics Express Vol. 27, Issue 3, pp. 2235-2247 (2019)
https://doi.org/10.1364/OE.27.002235

11 Raman imaging through multimode sapphire fiber

Sunan Deng, Damien Loterie, Georgia Konstantinou, Demetri Psaltis, and Christophe Moser
Optics Express Vol. 27, Issue 2, pp. 1090-1098 (2019)
https://doi.org/10.1364/OE.27.001090

12 Aberration correction for improving the image quality in STED microscopy using the genetic algorithm

Luwei Wang, Wei Yan, Runze Li, Xiaoyu Weng, Jia Zhang, Zhigang Yang, Liwei Liu, Tong Ye und Junle Qu
Nanophotonics 2018; 7(12): 1971–1980, https://doi.org/10.1515/nanoph-2018-0133

13 Nonlinear generation of Airy vortex beam

Hui Li, Haigang Kiu, Xianfeng Chen
Optics Express Vol. 26m Issue 16, 2018, https://doi.org/10.1364/OE.26.021204

14 Multiple-plane image formation by Walsh zone plates

Federico Machado, Vicente Ferrando, Fernando Gimenez, Walter D. Furlan, Juan A. Monsoriu
Optics Express Vol. 26, Issue 16, 2018, https://doi.org/10.1364/OE.26.021210

15 Wide-field in situ multiplexed Raman imaging with super resolution

Houkai Chen, Xiaojing Wu, Yuquan Zhang, Yong Yang, Changjun Min, Siwei Zhu, Xiaocong Yuan, Qiaoliang Bao, Jing Bu
Photonics Research Vol. 6, Issue 6, 2018, https://doi.org/10.1364/PRJ.6.000530

16 Observing the cell in its native state: Imaging subcellular dynamics in multicellular organisms

Tsung-Li Liu, Srigokul Upadhyayula, Daniel E. Milkie, Ved Singh, Kai Wang, Ian A. Swinburne, Kihore R. Mosaliganti, Zach M. Collins, Tom W. Hiscock, Jamien Shea, Abraham Q. Kohrman, Taylor N. Medwig, Daphne Dambournet, Ryna Forster, Brian Cunniff, Yuan Ruan, Hanako Yashiro, Steffen Scholpp, Ellio M. Meyerowitz, Dirk Hockemeyer, David G. Drubin, Benjamin L. Martin, David Q. Matus, Minoru Koyama, Sean G. Megason, Tom Kirchhausen, Eric Betzig
Science 20 Apr 2018, Vol. 360, Issue 6386, DOI: 10.1126/science.aaq1392

17 Far-field imaging of non-fluorescent species with sub-diffraction resolution

Pu Wang, Mikhail N. Slipchenko, James Mitchell, Chen Yang, Eric O. Potma, Xianfan Xu, Ji-Xin Cheng
Nature Photonics 7, 449-453 (2013) https://doi.org/10.1038/nphoton.2013.97

3.3 Wavefront correction and processing

One of features, which Spatial Light Modulators could provide is modifying optical fields in terms of amplitude, phase or both in the same time. Parameters like resolution and fill factor of each pixel are under investigation and improvement in newest laboratory experiments.

Thanks to phase modulation of light in the SLM plane, it is possible to correct aberrations present in optical setup. Most popular method to correct an incoming wavefront is to use a set of Zernike polynomials coefficients. With newest applications it is very important to adapt to actual conditions in real time. Thanks to SLMs features it is easily achievable.

Industry applications: Microscopy, Imaging

3.3.1 Publications and References

1 Chromatic aberration control with liquid crystal spatial phase modulators

Jose L. Martinez, Enrique J. Fernandez, Pedro M. Prieto, and Pablo Artal
Optics Express Vol. 25, Issue 9, pp. 9793-9801 (2017), https://doi.org/10.1364/OE.25.009793

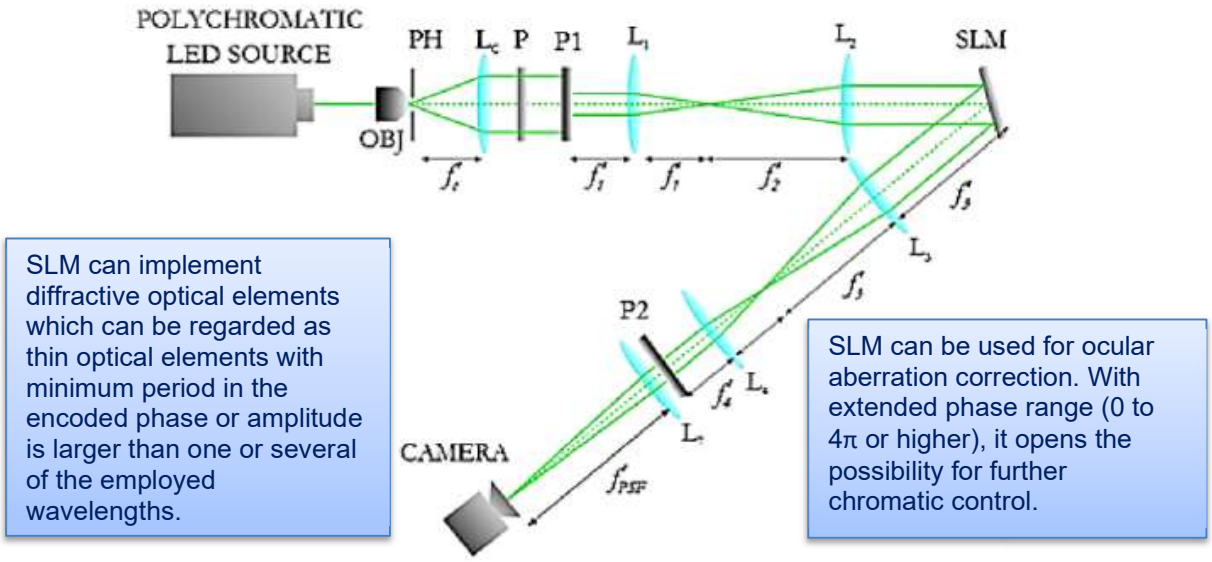

*Figure 34: Experimental setup used for obtaining the spectral response of a phase profile programmed into the SLM. **OBJ**: microscope objective. **PH:** pinhole aperture. **Lc:** collimating lens. **P:** polarizer.**P1, P2:** conjugated pupil planes. **L1-L2** and **L3-L4**: relay telescope. **L7, PSF** – generating lens*

Above image courtesy of Deng Pan, Bing Xu, Shunli Liu, Jiawen Li, Yanlei Hu, Dong Wu, Jiaru Chu. “Chromatic aberration control with liquid crystal spatial phase modulators” (2017)

2 Wavefront-shaping-based correction of optically simulated cataracts

Augusto Arias and Pablo Artal
Optica Vol. 7, Issue 1, pp. 22-27 (2020), https://doi.org/10.1364/OPTICA.7.000022

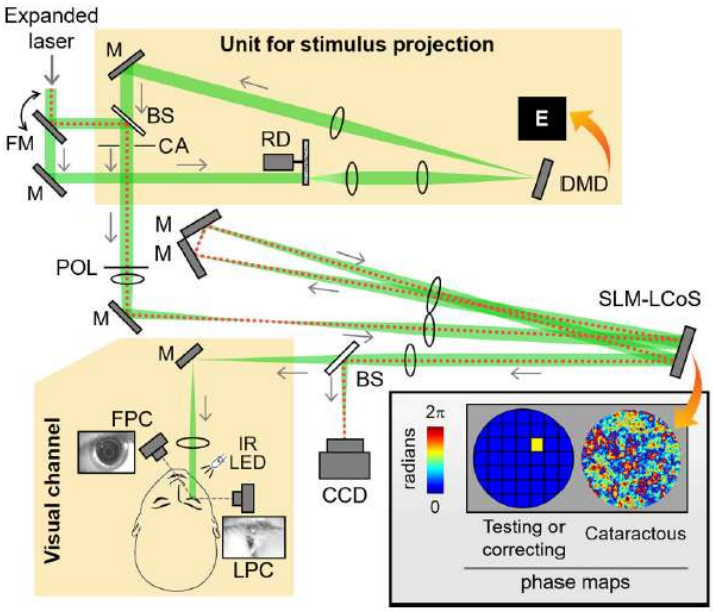

Figure 35: Experimental setup for the simultaneous generation and compensation of the effects of intraocular straylight. Label descriptions: FM, flip mirror; M, mirror; RD, rotating diffuser; BS, beam splitter; CA, circular aperture; POL, linear polarizer; IR LED, infrared light-emitting diode; FPC and LPC, frontal and lateral pupil cameras, respectively. The red dotted line depicts the path of the beam during the feedback-based WS correction.

Above image courtesy of Augusto Arias and Pablo Artal. “Wavefront-shaping-based correction of optically simulated cataracts” (2019)

3 Wavefront correction in two-photon microscopy with a multi-actuator adaptive lens

Juan M. Bueno, Martin Skorsetz, Stefano Bonora, and Pablo Artal
Optics Express Vol. 26, Issue 11, pp. 14278-14287 (2018),
https://doi.org/10.1364/OE.26.014278

SLM used in wavefront sensor-less technique to improve multiphoton microscopy images.

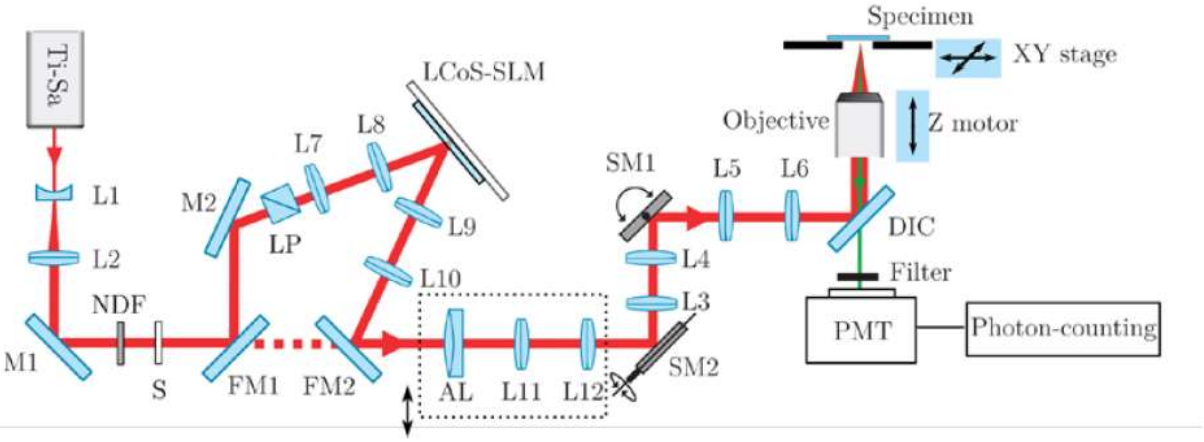

Figure 36: Above: Schematic diagram of the experimental setup. L1-L12: lenses. M1-M5: mirrors. FM1, FM2: flip mirrors. SM1, SM2: scanning mirrors. NDF: neutral density filter. DIC: dichroic mirror. PMT: photo-multiplier tube.

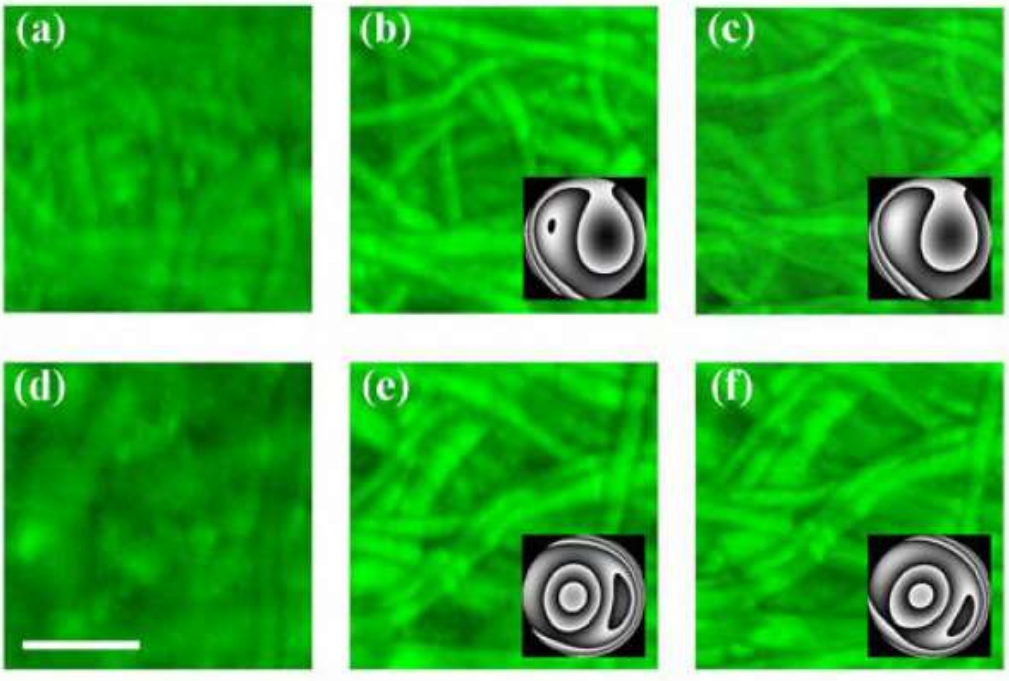

Figure 247: Comparison of improved multiphoton images using adaptive lens (AL) and LCoS SLM. (a)(d): original images, (b)(e): optimum images with AL, (c)(f): optimum images with LCoS. The insets correspond to the wavefront aberration that optimize the images. Dept locations: 50 µm (upper), 100 µm (bottom). Scale bar: 50 µm.

Above images courtesy of Juan M. Bueno, Martin Skorsetz, Stefano Bonora and Pablo Artal. “Wavefront correction in two-photon microscopy with a multi-actuator adaptive lens.” (2018)

More related publications:

4 Aberration correction for improving the image quality in STED microscopy using the genetic algorithm

Luwei Wang, Wei Yan, Runze Li, Xiaoyu Weng, Jia Zhang, Zhigang Yang, Liwei Liu, Tong Ye und Junle Qu
Nanophotonics 2018; 7(12): 1971–1980, https://doi.org/10.1515/nanoph-2018-0133

5 Adaptive wavefront interferometry for unknown free-form surfaces

Shuai Xue, Shanyong Chen, Zhanbin Fan, Dede Zhai
Optics Express, Vol. 26, Issue 17, 2018, https://doi.org/10.1364/OE.26.021910

6 Shaping the on-axis intensity profile of generalized Bessel beams by iterative optimization methods

Runze Li, Xianghua Yu, Tong Peng, Yanlong Yang, Baoli Yao, Chunmin Zhang, Tong Ye
Journal of Optics, Volume 20, Number 8, 2018, https://doi.org/10.1088/2040-8986/aace46

3.4 Holographic Optical Tweezer

Optical tweezers allow to trap a microscopic object of nano- or micrometer size by gradient forces and move it precisely. Many applications require the ability to control more than one object simultaneously.

Holographic optical tweezers (HOT) extend the basic principle of optical tweezers towards the optical control of a multitude of particles. Using SLMs one can modulate the phase-front of a laser light field spatially by means of computer generated holograms (CGH) in order to create several single tweezers in the microscopic sample at the same time.

Industry applications: Cell sorting, Drug development, micro rotator,

3.4.1 Publications and References

1 In situ single-atom array synthesis using dynamic holographic optical twee

Hyosub Kim, Woojun Lee, Han-gyeol Lee, Hanlae Jo, Yunheung Song & Jaewook Ahn
Nature Communications volume 7, Article number: 13317 (2016)
https://doi.org/10.1038/ncomms13317

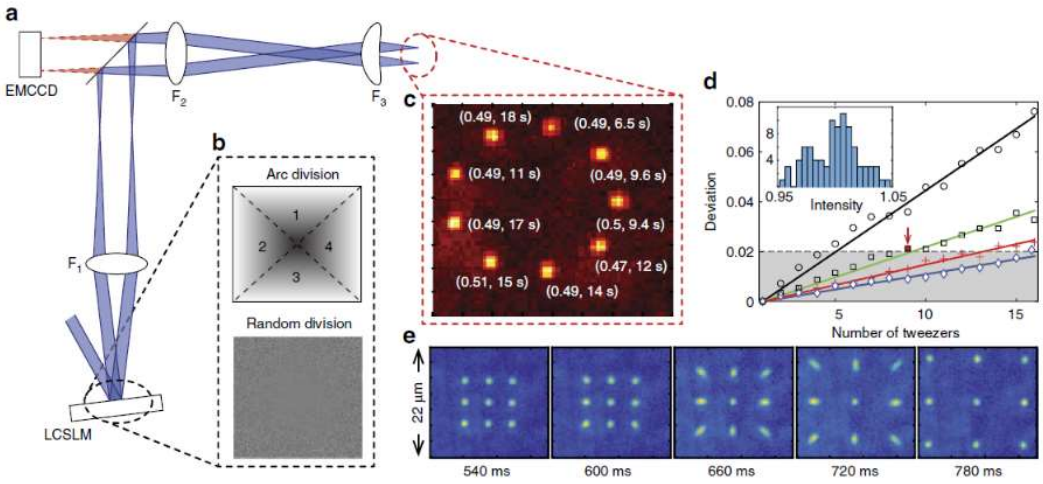

Figure 258: Setup for single-atom holographic transport. (a) The optical system for hologram transfer and trap imaging. (b) Schematic representation of 2D phase planes of the LC-SLM on the grey scale. (c) An example of loaded single atoms in a tweezer array, represented with 22 x 22 μm^2 size 500 cumulative images. (d) The intensity standard deviation as a function of N, for the random division. The data points were calculated for various beam waists W at the SLM window and the solid lines are the linear fits to the data. (e) An in situ single atom array expansion movie.

Above image courtesy of Kim, Hyosub and Lee, Woojun and Lee, Han-gyeol and Jo, Hanlae and Song, Yunheung and Ahn, Jaewook. “In situ single-atom array synthesis using dynamic holographic optical tweezers” (2016)

2 Calibration of spatial light modulators suffering from spatially varying phase response

David Engström, Martin Persson, Jörgen Bengtsson, and Mattias Goksör
Optics Express Vol. 21, Issue 13, pp. 16086-16103 (2013),
https://doi.org/10.1364/OE.21.016086

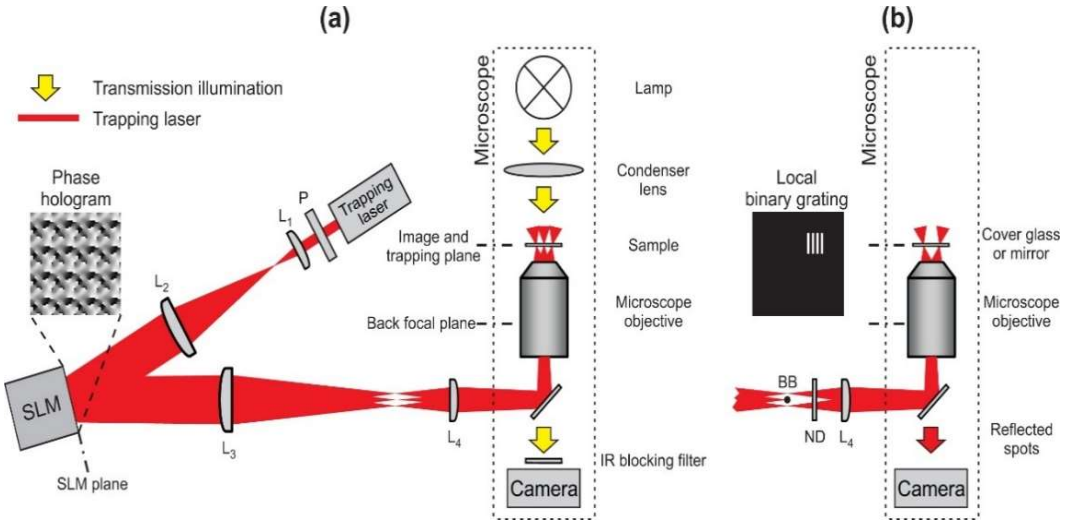

Figure 39: (a) The HOT setup is composed of a laser (λ =1070 nm), a polarizer (P), plano-convex lenses L_1 (focal length 150 mm), L_2 (120 mm), L_3 (400 mm), and L_4 (300 mm) with anti-reflection coating, an SLM, a microscope objective, and a camera. A halogen lamp, a condenser lens, and an IR blocking filter enable bright field imaging. (b) During characterization the SLM was locally addressed with binary gratings, the 0th order was blocked outside the microscope using a beam block (BB), bright field illumination was turned off, and the IR blocking filter was removed to allow detection of the laser light reflected off a cover glass or mirror. For $P_{SLM} \geq 0.5$ W, a reflective ND filter was also inserted outside the microscope to decrease the power reaching the camera.

Above image courtesy of David Engstrom, Martin Persson, Jorgen Bengtsson, Mattias Goksor "Calibration of spatial light modulators suffering from spatially varying phase response" (2013)

3 Parid tilted-plane Gerchberg-Saxton algorithm for holographic optical tweezers

Yanan Cai, Shaohui Yan, Zhaojun Wang, Runze Li, Yansheng Liang, Yuan Zhou, Xing Li, Xianghua Yu, Ming Lei, and Baoli Yao
Optics Express Vol. 28, Issue 9, pp. 12729-12739 (2020), https://doi.org/10.1364/OE.389897

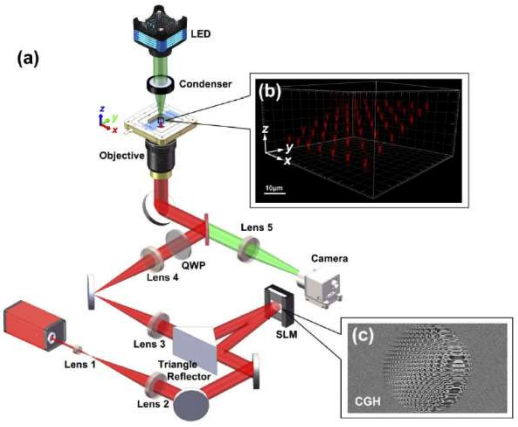

Figure 40: (a) Schematic of the home built holographic optical tweezers. (b) Experimentally measured 3D intensity profile of the foci array. (c) The Computer Generated Hologram for the foci array

Above image courtesy of Yanan Cai, Shaohui Yan, Zhaojun Wang, Runze Li, Yansheng Liang, Yuan Zhou, Xing Li, Xianghua Yu, Ming Lei, Baoli Yao. „Parid tilted-plane Gerchberg-Saxton algorithm for holographic optical tweezers" (2020)

More related publications:

4 Experimental Optical Trapping Of Micro-particles With Frozen Waves

Rafael A. B. Suarez, Leonardo A. Ambrosio, Antonio A. R. Neves, Michel Zamboni-Rached Marcos R. R. Gesualdi
Optics Letters, Vol. 45, issue 9, 2020, https://doi.org/10.1364/OL.390909

5 Rapid Tilted-plane Gerchberg-Saxton Algorithm For Holographic Optical Tweezers

Yanan Cai, Shaohui Yan, Zhaojun Wang, Runze Li, Yansheng Liang, Yuan Zhou, Xing Li, Xianghua Yu, Ming Lei, Baoli Yao
Optics Express, 2020, https://doi.org/10.1364/oe.389897

6 Generation Of Tunable Fractional Vector Curvilinear Beams With Controllable Phase Distribution

Fengyan Gu, Zhongzheng Gu, Chenliang Chang, Caojin Yuan, Shaotong Feng, Fangjian Xing, Shouping Nie
Photonics Journal, Volume 11, Number 6, 2019, DOI: 10.1109/JPHOT.2019.2942041

7 Generation of Reconfigurable Optical Traps for Microparticles Spatial manipulation Through Dynamic Split Lens Inspired Light Structures

Angel Lizana, Haolin Zhang, Alex Turpin, Albert Van Eeckhout, Fabia A. Torres-Ruiz, Asticio Vargas, Claudio Ramirez, Francesc Pi, Juan Campos
Scientific Reports, 2018, DOI: 10.1038/s41598-018-29540-1

8 Micro-Dumbbells – A Versatile Tool For Optical Tweezers

Weronika Lamperska, Slawomir Drobczynski, Michal Nawrot, Piotr Wasylczyk, Jan Masajada 2018, DOI: 10.20944/preprints201805.0185.v1

9 Particle trapping and conveying using an optical Archimedes screw

Barak Hadad, Sahar Froim, Harel Nagar, Tamir Admon, Yaniv Eliezer, Yael Roichman, Alon Bahabad
Optica, Vol. 5, No. 5, 2018, https://doi.org/10.1364/OPTICA.5.000551

10 Investigation of albumin-derived perfluorocarbon-based capsules by holographic optical trapping

Jannis Köhler, Jegor Ruschke, Katja Bettina Ferenz, Cemal Esen, Michael Kirsch, Andreas Ostendorf
Biomedical Optics Express, Vol. 9, No. 2, 2018, DOI:10.1364/BOE.9.000743

11 Rotating of low-refractive-index microparticles with a quasi-perfect optical vortex

Yansheng Liang, Ming Lei, Shaohui Yan, Manman Li, Yanan Cai, Zhaojun Wang, Xianghua Yu, Baoli Yao
Applied Optics, Vol. 57, No. 1, 2018, https://doi.org/10.1364/ao.57.000079

12 Fast label-free microscopy technique for 3D dynamic quantitative imagining of living cells

Jose A. Rodrigo, Juan M. Soto, Tatiana Alieva
Biomedical Optics Express, Vol. 8, Issue 12, , https://doi.org/10.1364/BOE.005507

3.5 Beam shaping with structured light

Control of laser beam irradiance profile, particularly providing uniform distribution, is of great importance for various holography applications based on SLMs.

A specific demand of SLM illumination in these techniques is in strict requirements to flatness of phase front of a laser beam that should be conserved while any irradiance profile transformations, i.e. flatness of both phase front and irradiance distribution should be realized simultaneously.

Industry applications: 3D scanners, Imaging Technologies, Free Space Communication, Microscopy, Holographic Optical Tweezers, Material Processing

3.5.1 Publications and References

1 Creation and detection of optical modes with spatial light modulators

Andrew Forbes, Angela Dudley, and Melanie McLaren
Advances in Optics and Photonics Vol. 8, Issue 2, pp. 200-227 (2016),
https://doi.org/10.1364/AOP.8.000200

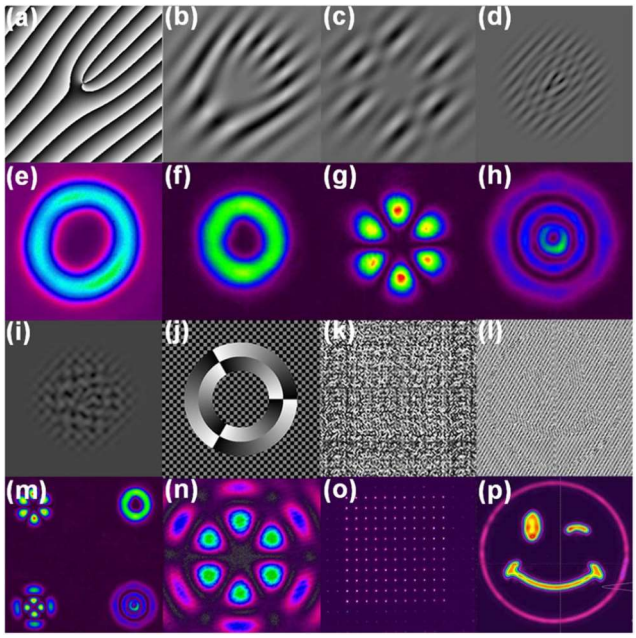

Figure 41: Examples of digital holograms employing various methods for the creation of structured light fields: (a) azimuthal phase-only (b) Laguerre Gaussian amplitude with azimuthal phase (c) amplitude modulation to produce a superposition state of two azimuthal modes (d) complex amplitude modulation for radial mode control (i) multiplexed holograms to produce four modes or various radial and azimuthal indices (j) azimuthal phase-only slits with a checkerboard to define the zero transmission regions (k) hologram as a result of an iterative approach (l) complex amplitude modulation to produce an arbitrary desired field. The experimental realization of each hologram is shown as the corresponding image below.

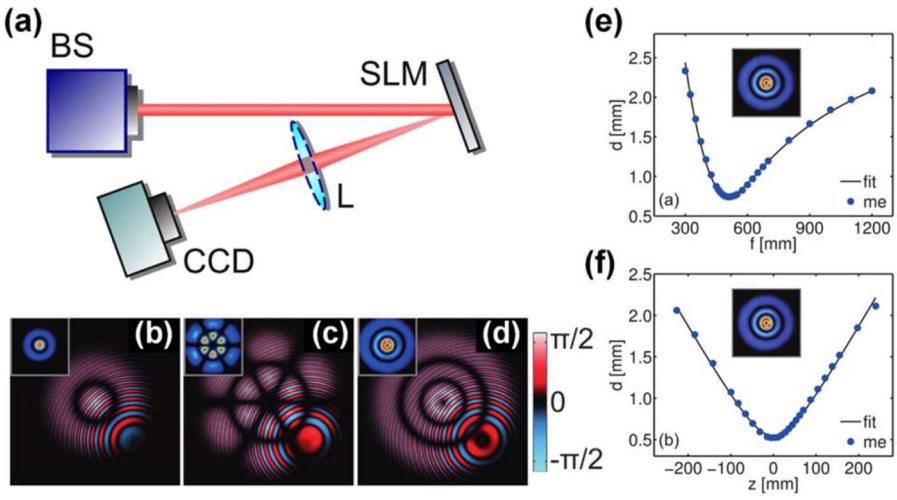

Figure 42: (a) Experimental approach to digitally propagate light, with all elements static, where BS denotes beam source and CCD is a charged-coupled device. (b)-(d) Examples of holograms for mode creation and propagation. (e)(f) measured and calculated propagation data for Laguerre-Gaussian beams using the digital lens and digital propagation approaches.

Above images courtesy of Andrew Forbes, Angela Dudley, Melanie McLaren. „Creation and detection of optical modes with spatial light modulators“. (2016)

2 Lossless reshaping of structured light

Stirling Scholes, Valeria Rodríguez-Fajardo, and Andrew Forbes
Journal of the Optical Society of America A Vol. 37, Issue 11, pp. C80-C85 (2020),
https://doi.org/10.1364/JOSAA.394807

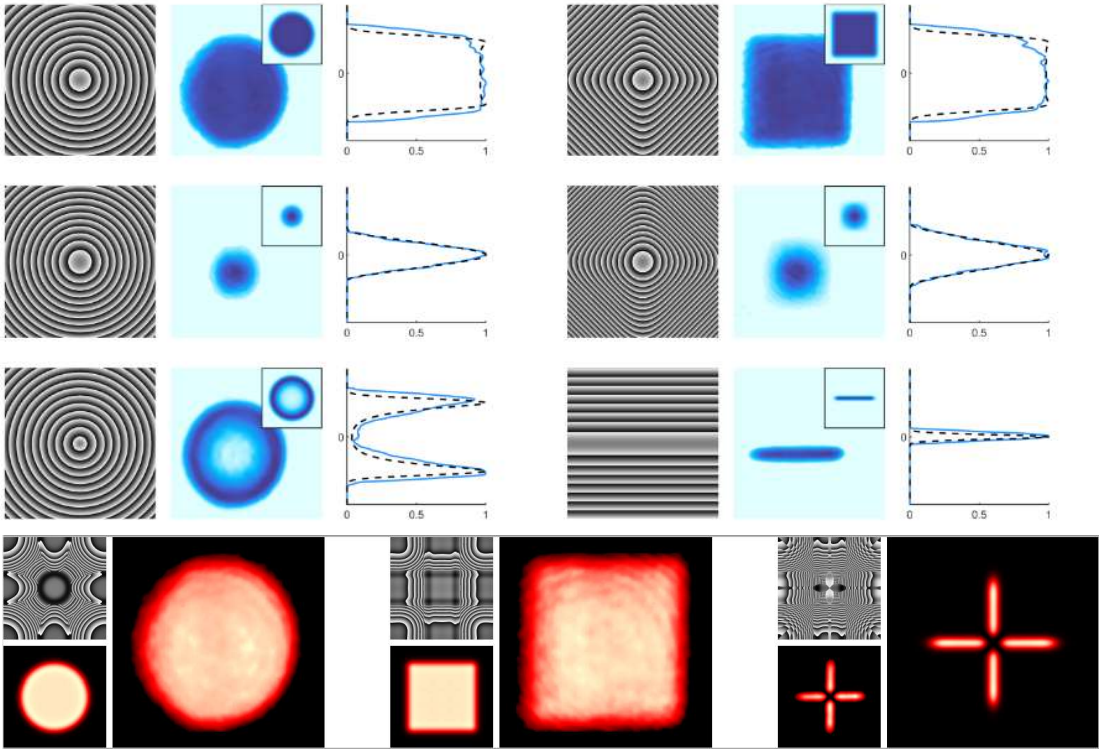

Figure 43: Measured modes and profiles for beams with Radial and Cartesian symmetry. Each row of the figure shows from left to right, the phase of the first shaping element, the experimentally measured beam, and a comparison of the profiles of the simulated and measured beams as a black dashed line and blue solid line respectively. The insets in each experimental result show the simulated beam.

Above images courtesy of Stirling Scholes, Valeria Rodriguez-Fajardo and Andrew Forbes. „Lossless reshaping of structured light“ (2020)

3 Generation of complex transverse energy flow distributions with autofocusing optical vortex beams

Svetlana N. Khonina, Alexey P. Porfirev, Andrey V. Ustinov, Muhammad Ali Butt
Micromachines 2021, 12, 297
https://doi.org/10.3390/mi12030297

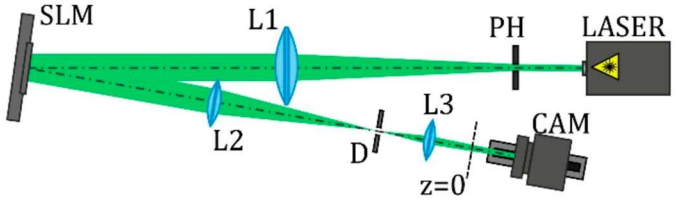

Figure 44: Experimental setup for the investigation of the generation and propagation of designed autofocusing optical vortex beams. PH: pinhole (40μm), L1-L3: lenses, SLM: Spatial Light Modulator, D: circular aperture, CAM: video camera

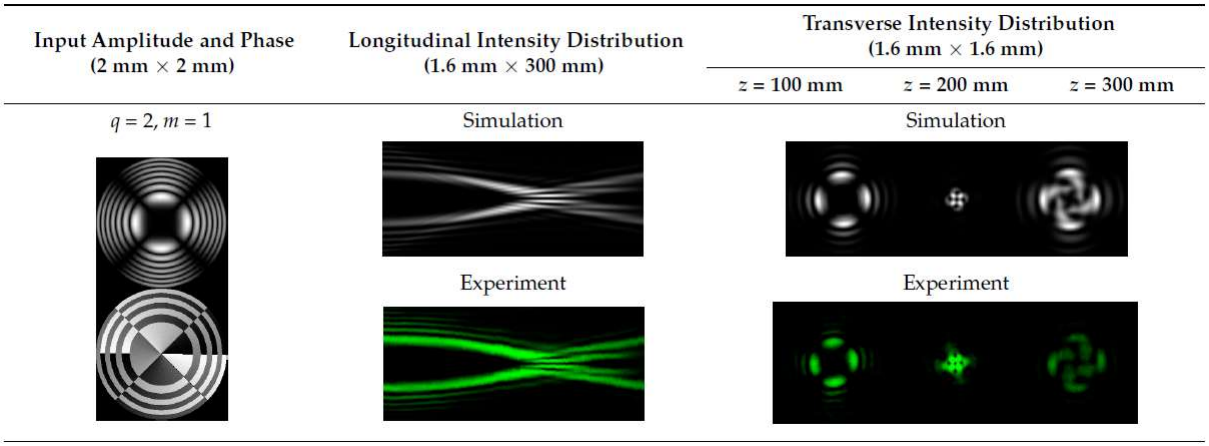

Figure 265: Results of modeling and experiment for the filed defined by equation with azimuthal modulation of order q=2 with different orders of additional vortex phase singularity m.

Above images courtesy of Svetlana N. Khonina, Alexey P. Porfirev, Andrey V. Ustinov, Muhammad Ali Butt.
„Generation of complex transverse energy flow distributions with autofocusing optical vortex beams“ (2021)

4 Tailoring a complex perfect optical vortex array with multiple selective degress of freed

Hao Wang, Shiyao Fu, Chunqing Gao
Optics Express, Vol. 29, No. 7, 29 March 2021
https://doi.org/10.1364/OE.422301

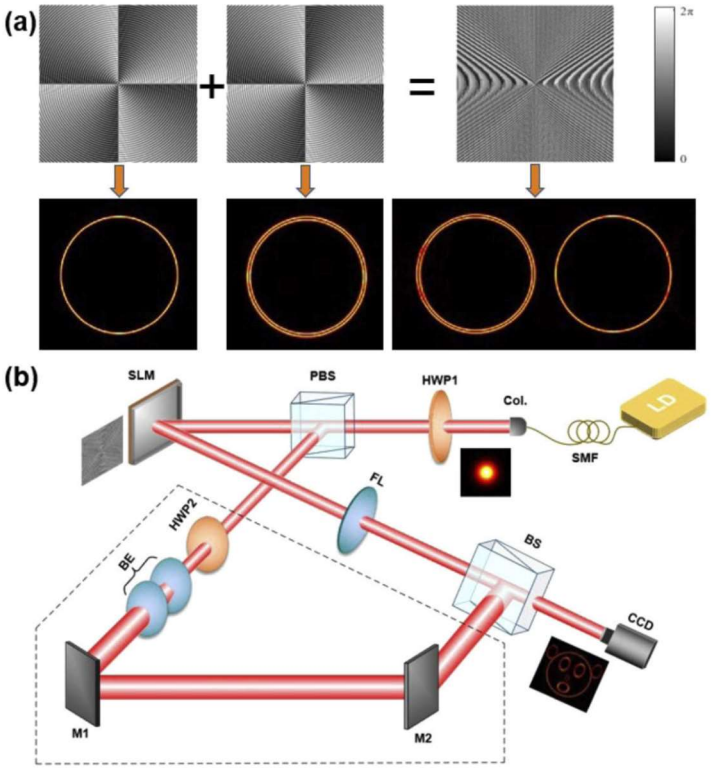

Figure 46: (a) General formation of holographic grating to produce POV array. (b) The experimental layout. LD: laser diode, SMF: single mode fiber, COL: collimator, HWP1-2: half wave plate, PBS: polarized beam splitter, SLM: spatial light modulator, FL: Fourier lens, BE: beam expander, M1-2: mirrors, BS: beam splitter, CCD: infrared CCD camera. The content of the dotted box in subfigure (b) is the interference optical path.

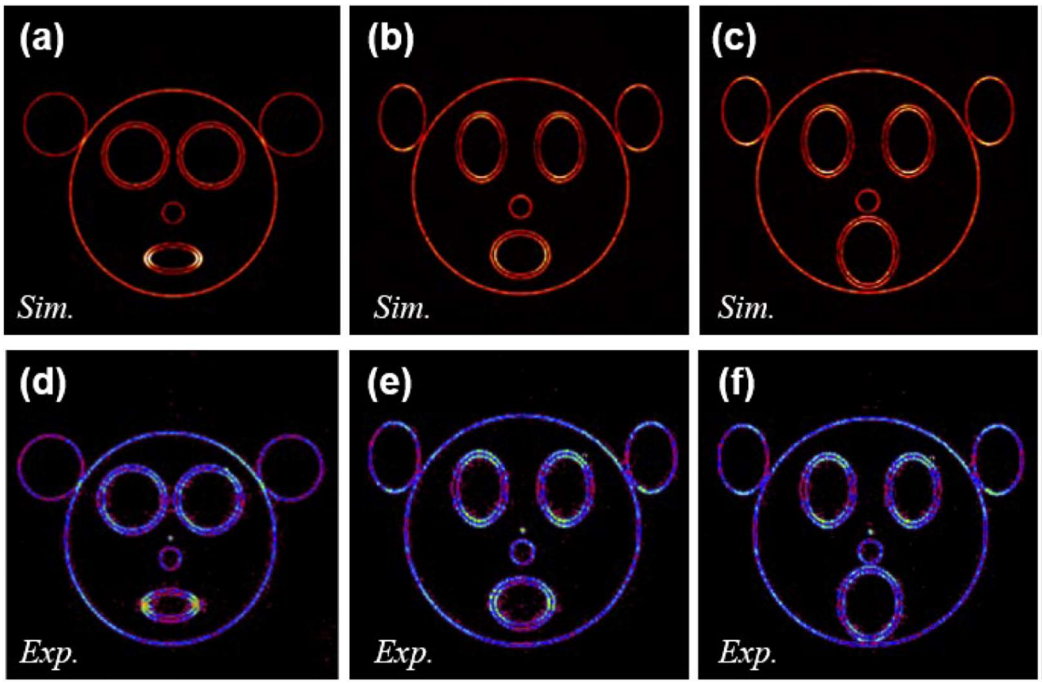

Figure 47: Simulated and experimental results of the Bear POV. The "bear" becomes more astonished from left to right.

More related publications:

5 Generation of composite vortex beams by independent Spatial Light Modulator pixel addressing
Mateusz Szatkowski, Jan Masajada, Ireneusz Augustyniak, Klaudia Nowacka
Optics Communications, 463, 2020,https://doi.org/10.1016/j.optcom.2020.125341

6 Amplitude-phase optimized long depth of focus femtosecond axilens beam for single-exposure fabrication of high-aspect-ratio microstructures
Deng Pan, Bing Xu, Shunli Liu, Jiawen Li, Yanlei Hu, Dong Wu, Jiaru Chu
Optics Letters, Vol. 45, No. 9, 2020 https://doi.org/10.1364/ol.389946

7 Three-dimensional tomography of red blood cells using deep learning
Joowon Lim, Ahmed B. Ayoub, Demetri Psaltis
Advanced Photonics, 2020, DOI: 10.1117/1.AP.2.2.26001

8 Polarization nano-tomography of tightly focused light landscapes by self-assembled monolayers
Eileen Otte, Kemal Tekce, Sebastian Lamping, Bart Jan Ravoo, Cornelia Denz
Nature Communications 10, Article number: 4308, 2019
https://doi.org/10.1038/s41467-019-12127-3

9 Chain of optical vortices synthesized by a Gaussian beam and the double-phase-ramp converter
Anna Khoroshun, Oleksii Chernykh, Halyna Tatarchenko, Shunichi Sato, Yuichi Kozawa, Agnieszka Popiolek-Masajada, Mateusz Szatkowski, Weronika Lamperska
OSA Continuum, Vol. 2, 2019, DOI: 10.1364/osac.2.000320

10 Measuring orbital angular momentum of light based on petal interference patterns
Shengzhe Pan, Chunying Pei, Shuang Liu, Jin Wei, Di Wu, Zhanou Liu, Yaling Yin, Yong Xia, Jianping Yin
OSA Continuum, Vol. 1, 2018, DOI: 10.1364/osac.1.000451

11 Laser surface structuring of diamond with ultrashort Bessel beams
Sanjeev Kumar, Shane M. Eaton, Monica Bollani, Belen Sotillo, Andrea Chiappini, Maurizio Ferrari, Roberta Ramponi, Paolo Di Trapani, Ottavia Jedrkiewicz
Scientific Reports, 2018, DOI: 10.1038/s41598-018-32415-0

3.6 Higher Order Generation

Higher order mode generation is a standard application for phase only SLMs. Even though this finds also use for e.g. HOT and beam shaping that are discussed earlier we decided to treat it in a separate chapter due to its high interest for the optical community.

Examples for higher order modes are Laguerre Gaussian (LG) modes, airy beams and Bessel beams. LG modes that are circular symmetric can be generated by vortex functions and carry orbital angular momentum, what makes them suitable for optical trapping, STED microscopy and also multiplexing in free space communication applications.

Airy beams as propagation invariant wave propagates along a curved parabolic route and are also self-healing, meaning that they are resistant against disturbances in the optical beam path comparable to Bessel beams that is a non-diffracting beam, what means that it does not diffract while propagating and does not spread out quickly after being focused. These properties enable a wide variety of different applications for e.g. imaging and microscopy.

Industry applications: Microscopy, Optical trapping, Free Space Communication, Imaging

3.6.1 Publications and References

1 Vectorial optical field generator for the creation of arbitrarily complex fields

Wei Han, Yanfang Yang, Wen Cheng, Qiwen Zhan
Optics Express 21(18):20692-20706,
dx.doi.org/10.1364/OE.21.020692

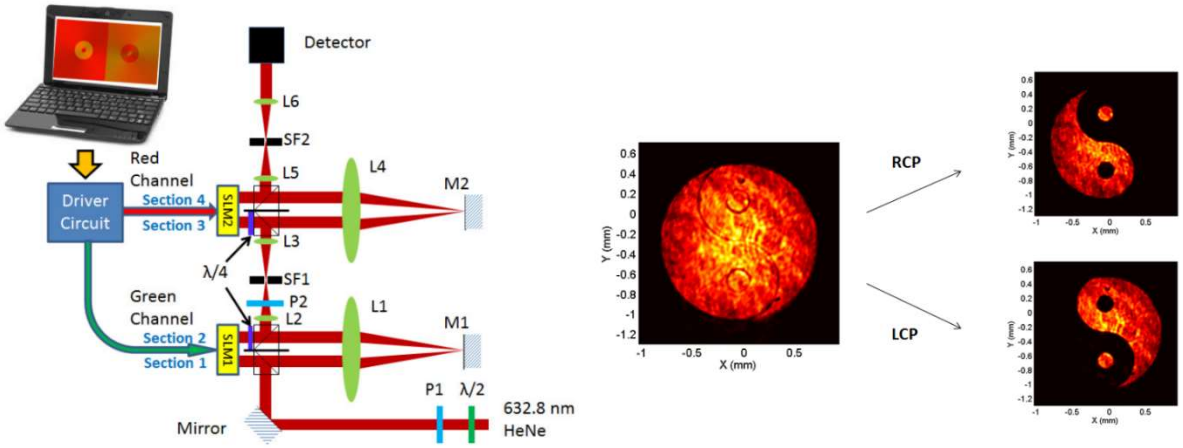

Figure 48: (Left) Schematic diagram of the experimental setup for the Vectorial Optical Field Generation. (Right) Taiji pattern coded in circular polarization. The total field, the upper half Taiji pattern in Right-hand Circular Polarization and the lower half Taiji pattern in Left-hand Circular Polarization.

Above images courtesy of Wei Han, Yanfang Yang, Wen Cheng, Qiwen Zhan „ Vectorial optical field generator for the creation of arbitrarily complex fields “ (2013)

2 Non-interferometric technique to realize vector beams embedded with polarization singularities

Praveen Kumar, Sushanta Kumar Pal, Naveen K. Nishchal, and P. Senthilkumaran
Journal of the Optical Society of America A Vol. 37, Issue 6, pp. 1043-1052 (2020), https://doi.org/10.1364/JOSAA.393027

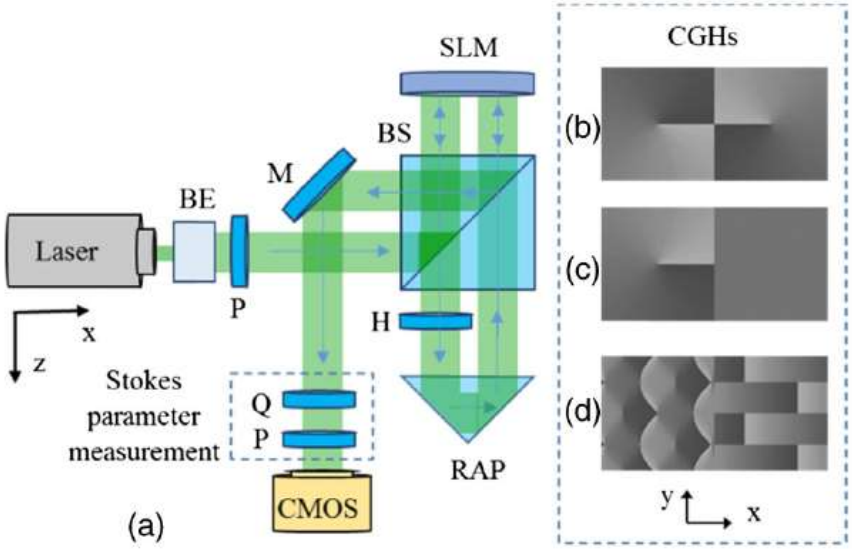

Figure 49: (a) Schematic of the experimental setup. BE: beam expander. P: polarizer. M: Mirror. SLM: Spatial Light Modulator. BS: beam splitter. H: half-wave plate. RAP: right-angle prism. Q: quarter-wave plate. CMOS: complementary metal-oxide semiconductor. CGH: computer generated holograms for (b) V-point of Type I, (c) star-type C-point, and (d) azimuthal-star-type lattice field.

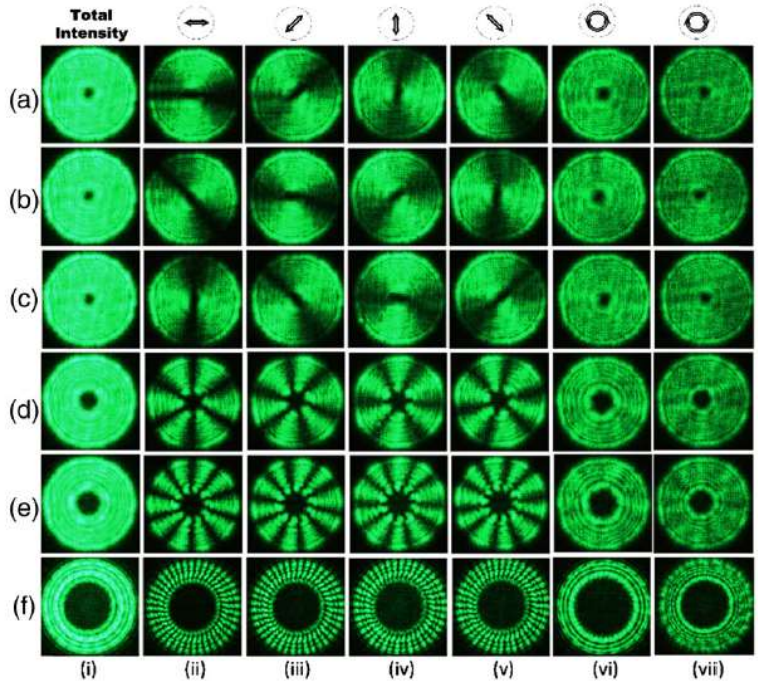

Figure 50: Experimentally recorded intensity distributions for vector beams having V-points. Rows present (a) azimuthal (b) spiral (c) radial polarization distributions. (d)-(f) Hiher-order radial distributions of order 3rd, 5th and 20th. Column (i) shows the total intensity, and columns (ii)-(vii) show the intensity when the field is analyzed using a linear polarizing filter (four different orientations) and two circular polarizing filters.

Above image courtesy of Praveen Kumar, Sushanta Kumar Pal, Naveen K. Nishchal, P. Senthilkumaran. „Non-interferimetric technique to realize vector beams embedded with polarization singularities“ (2020)

3 Generating superpositions of higher–order Bessel beams

Ruslan Vasilyeu, Angela Dudley, Nikolai Khilo, and Andrew Forbes
Optics Express Vol. 17, Issue 26, pp. 23389-23395 (2009),
https://doi.org/10.1364/OE.17.023389

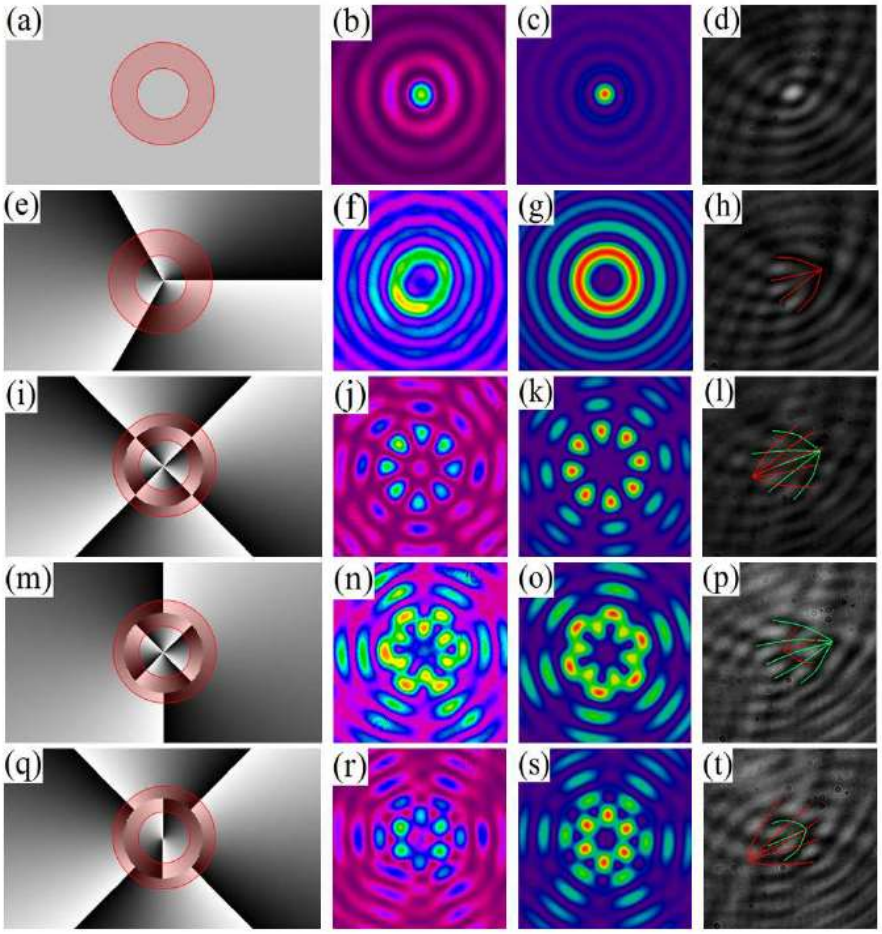

Figure 51: The columns from left to right represent the phase patterns applied to the liquid crystal display of the SLM, the observed intensity distribution of the superposition, the theoretical prediction, and interference pattern of the superposition field and a plane wave, respectively.
Data is shown for (a)-(d): A0, (e)-(h): A3, (i)-(l): A4,-4, (m)-(p): A2,-4, (q)-(t): A4,-2.
The illuminated ring slit is shown as a shaded overlay on the phase pattern.

Above image courtesy of Ruslan Vasilyeu, Angela Dudley, Nikolai Khilo and Andrew Forbes. “Generating superpositions of higher-order Bessel beams” (2009)

4 Direct measurement of a 27-dimensiona orbital-angular-momentum state vector

Mehul Malik, Mohammad Mirhosseini, Martin Lavery, Jonathan Leach
Nature Communications 5(1):3115, DOI: 10.1038/ncomms4115

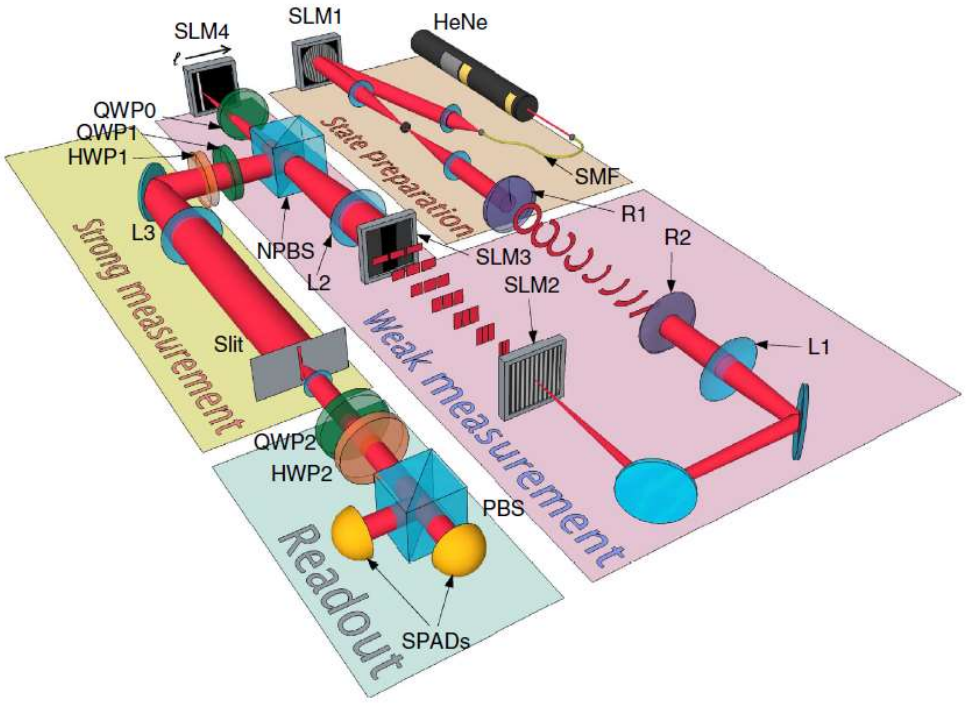

Figure 52: Experimental setup for direct measurement of a high-dimensional state vector.
State preparation: a quantum state in an arbitrary superposition of OAM modes is prepared by impressing phase information with SLM1 on spatially filtered (SMF) photons from an attenuated HeNe laser.
Weak measurement: a particular OAM mode is weakly projected by rotating its polarization. In order to do so, the OAM modes are first transformed into finite-sized momentum modes by two refractive optical elements made out of Poly methyl methacrylate (R1 and R2). Then, a Fourier transform lens (L1) and a fan-out hologram implemented on SLM2 are used to generate three adjacent copies of each momentum mode. The phase between these copies is corrected by SLM3. Another lens (L2) converts these larger momentum modes into well-separated position modes at its focus. Finally, a QWP0 used in double pass with SLM4 is used to rotate the polarization of the OAM mode to be weakly projected. Another QWP and HWP are used to remove any ellipticity introduced by transmission and reflection through the non-polarizing beam splitter.
Strong measurement: a strong measurement of angular position is performed by Fourier transforming with a lens (L3) and post-selecting state Θ=Θ0 with a 10 μm slit.
Readout: the OAM weak value ⟨π_l ⟩ is obtained by measuring the change in the photon polarization in the linear and circular polarization bases. QWP2, HWP1, a polarizing beam splitter (PBS) and two single-photon avalanche detectors (SPADs) are used for this purpose.

Above image courtesy of Mehul Malik, Mohammad Mirhosseini, Martin Lavery, Jonathan Leach. “Direct measurement of a 27-dimensiona orbital-angular-momentum state vector” (2014)

5 Asymetric Bessel-Gauss beams

V. V. Kotlyar, A. A. Kovalev, R. V. Skidanov, and V. A. Soifer
Journal of the Optical Society of America A Vol. 31, Issue 9, pp. 1977-1983 (2014), https://doi.org/10.1364/JOSAA.31.001977

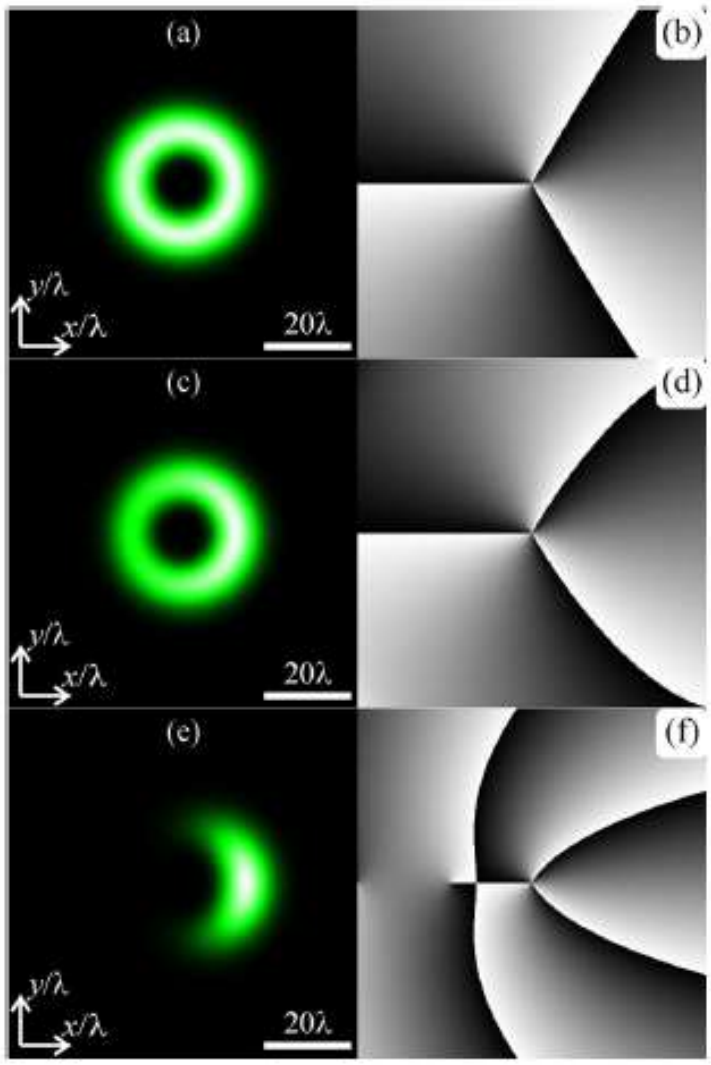

Figure 53: Intensity (a)(c)(e) and phase (b)(d)(f) patterns from the third-order beam equation at n=3, z=0 and different values of the asymmetry parameter c: (a), (b) 0.1; (c),(d) 1; and (e),(f) 10 .

Above image courtesy of V.V. Kotlyar, A.A. Kovalev, R.V. Skidanov, V. A. Soifer. “Asymetric Bessel-Gauss beams” (2014)

6 Holographic tool kit for optical communication beyond orbital angular momentum

Abderrahmen Trichili, Carmelo Rosales-Guzmán, Angela Dudley, Bienvenu Ndagano, Amine Ben Salem, Mourad Zghal, Andrew Forbes
SPIE Optical Engineering + Applications, 2016, DOI: 10.1117/12.2238416

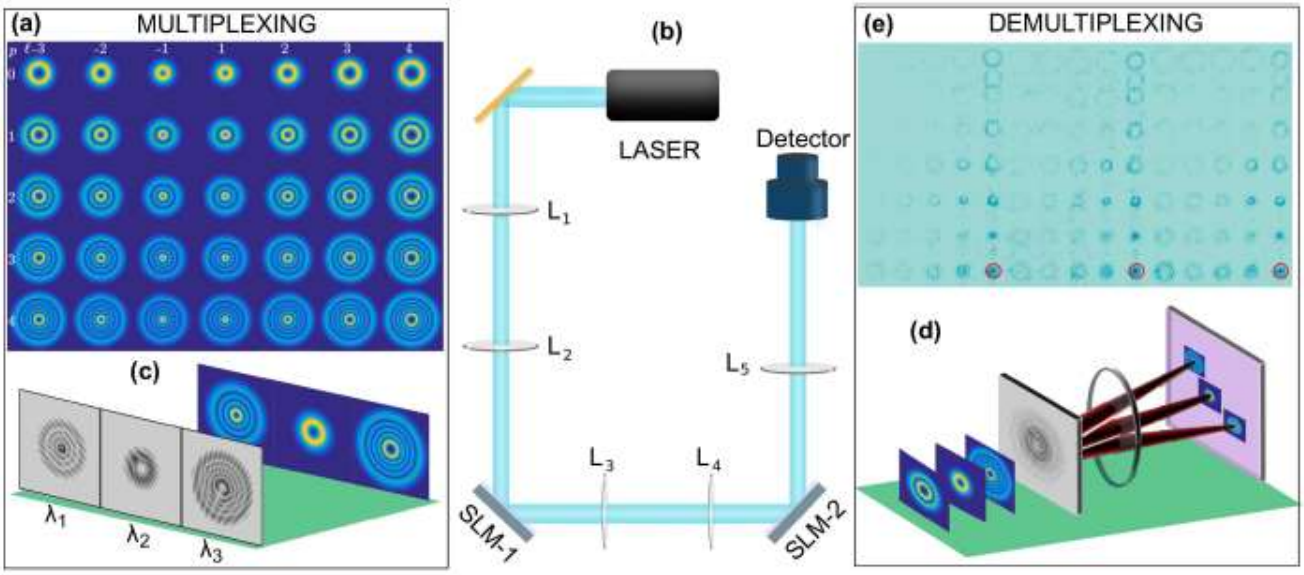

Figure 54: Schematic of Multiplexing and Demultiplexing setup.

(a) Intensity profiles of LG_{pl} modes generated from combinations of p = (0,1,2,3,4) and l=(-3,-2,-1,1,2,3,4).
(b) Experimental setup: Three components of a multiline Ion-Argon laser λ1 = 457 nm, λ2 = 488 nm, λ3 = 514 nm, are separated using a grating and sent to a Spatial Light Modulator (SLM-1)
(c) The SLM is split into three independent screens, and addressed with holograms to produce the set of modes shown in (a). The information is propagated through free space and reconstructed in the second stage with a modal filter.
(d) The modal filter consists of a superposition of all holograms encoded in SLM-2.
(e) Each mode is identified in the far filed using a CCD camera and a lens.

Above image courtesy of Carmelo Rosales-Guzman, Angela Dudley, Bienvenu Ndagano, Andrew Forbes, Abderrahmen Trichili, Amine Ben Salem, Mourad Zghal. “Holographic tool kit for optical communication beyond orbital angular momentum” (2016)

7 Non-diffracting and self-accelerating Bessel beams with on-demand tailored intensity profiles along arbitrary trajectories

Wenxiang Yan, Yuan Gao, Zheng Yunan, Zhuang Wang, Zhi-Cheng Ren, Xi-Lin Wang, Jianping Ding, Hui-Tian Wang
Optics Letters, April 2021, https://doi.org/10.1364/OL.418928

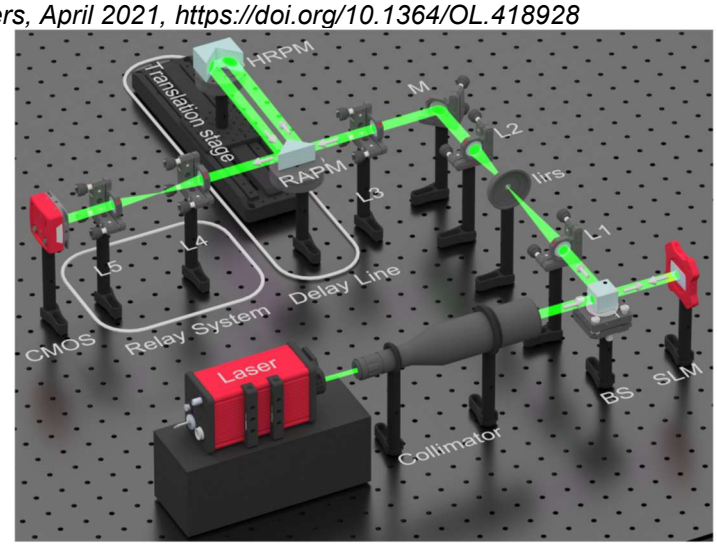

Figure 55: Experimental setup for generating and detecting Bessel beams with controllable self-accelerating trajectories and intensity profiles.BS: beam splitter, SLM: phase only spatial light modulator, L1-L5: lens, M: mirror, RAPM: right-angle prism mirror, HRPM: hollow roof prism mirror, CMOS: complementary metal oxide semiconductor camera

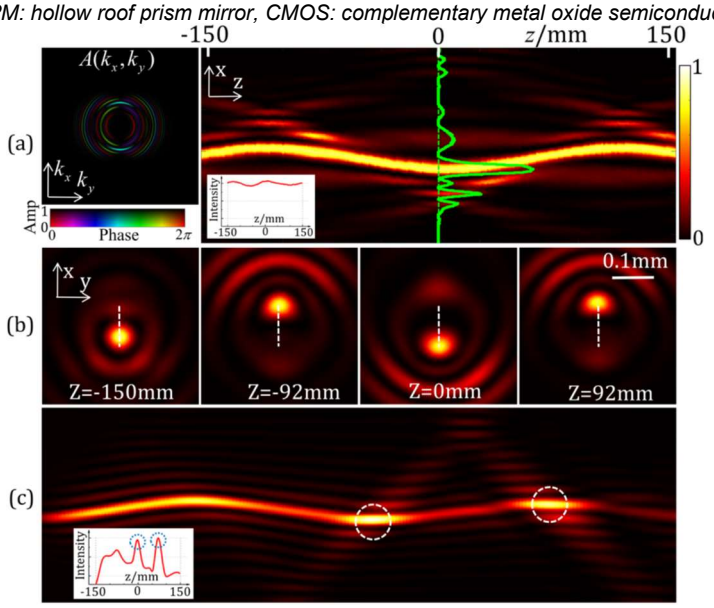

Figure 56: Generated accelerating snake Bessel beam with an uniform intensity distribution along the z direction.
(a) angular spectrum (left) and intensity map in the x-z plane (right)
(b) intensity map in the four x-y planes at z= -150 mm, -92 mm, 0 mm, 92 mm, respectively.
(c) Bessel beam generated by the method in ref [12]. The z-directional intensity profile of the Bessel beam's mainlobe is shown in the inset of (a) and (c).
Link to visualization: https://opticapublishing.figshare.com/articles/media/Visualization2_mp4/13521389

Above image courtesy of Wenxiang Yan, Yuan Gao, Zheng Yuan, Zhuang Wang, Zhi-Cheng Ren, Xi-Lin Wang, Jianping Ding, Hui-Tian Wang.
"Non-diffracting and self-accelerating Bessel beams with on-demand tailored intensity profiles along arbitrary trajectories" (2021)

More related publications:

8 Generating superpositions of higher-order Bessel beams

Ruslan Vasilyeu, Angela Dudley, Nikolai Khilo, Andrew Forbes
Optics Express, Vol. 17, No. 26, 2009

9 Airy transform of Laguerre-Gaussian beams

Guoquan Zhou, Fei Wang, Shangshen Feng
Optics Express, Vol. 28, Issue 13, https://doi.org/10.1364/OE.395982

10 Asymetric Bessel-Gauss beams

V.V. Kotlyar, A. A. Kovalev, R. V. Skidanov, V. A. Soifer
Journal of the Optical Society of Amercia A, Vol. 31, Issue 9,
https://doi.org/10.1364/JOSAA.31.001977

3.7 Material Processing

The use of the SLM technology opens up new possibilities for flexible beam shaping like the generation of flat-tops, multi-spot-arrays or arbitrary intensity distributions which can be used in the micro material processing.

Industry applications: Parallel laser drilling, Selective laser melting, Laser marking, Generation of complex photonic lattices

3.7.1 Publications and References

1 High efficiency fabrication of complex microtube arrays by scanning focused femtosecond laser Bessel beam for trapping/releasing biological cells

Liang Yang, Shengyun Ji, Kenan Xie, Wenqiang Du, Bingjie Liu, Yanlei Hu, Jiawen Li, Gang Zhao, Dong Wu, Wenhao Huang, Suling Liu, Hongyuan Jiang, and Jiaru Chu
Optics Express Vol. 25, Issue 7, pp. 8144-8157 (2017), https://doi.org/10.1364/OE.25.008144

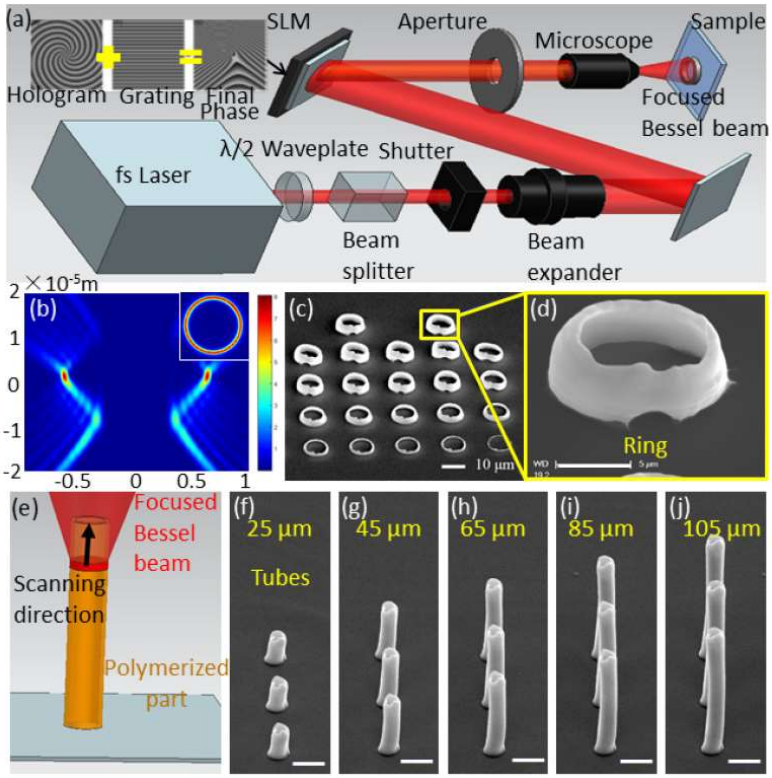

Figure 57: High efficiency fabrication of micro tubes by focused femtosecond laser Bessel beam scanning.
(a) Femtosecond Bessel beam is generated by phase modulation using a predesigned hologram loaded in the SLM. The inset shows the combination of blazed grating and hologram for a Bessel beam to separate the Bessel beam from the zero diffraction order.
(b) The intensity distribution at the focal region of a focused 20th order Bessel beam. The inset shows the intensity distribution at the focal plane.
(c) Cylindrical microstructures fabricated by ascending the focal plane line-by-line. In the fifth line, only two cylinders are left and this is the critical position where the cylinder adheres to the substrate.
(d) Magnified SEM images of polymerized cylindrical microstructure generated in a single shot. The scale bar is 5 μm.
(e) Schematic of the new strategy for rapid fabrication of micro tube by scanning focused Bessel beam.
(f)-(j) Micro tubes fabricated with height of 25 μm, 45 μm, 65 μm, 85 μm and 105 μm. Focused 20th order Bessel beam is used for single exposure of cylindrical microstructure in (c)-(d) and for the fabrication of micro tubes in (f)-(j). The scale bar are 20 μm.

Above image courtesy of Liang Yang, Shengyun Ji, Kenan Xie, Wenqiang Du, Bingjie Liu, Yanlei Hu, Jiawen Li, Gang Zhao, Dong Wu, Wenhao Huang, Suling Liu, Hongyuan Jiang, Jiaru Chu. „High efficiency fabrication of complex micro tube arrays by scanning focused femtosecond laser Bessel beam for trapping/releasing biological cells“ (2017)

2 High power, ultrashort pulse control through a multi-core fiber for ablation

Donald B. Conkey, Eirini Kakkava, Thomas Lanvin, Damien Loterie, Nicolino Stasio, Edgar Morales-Delgado, Christophe Moser, and Demetri Psaltis
Optics Express Vol. 25, Issue 10, pp. 11491-11502 (2017),
https://doi.org/10.1364/OE.25.011491

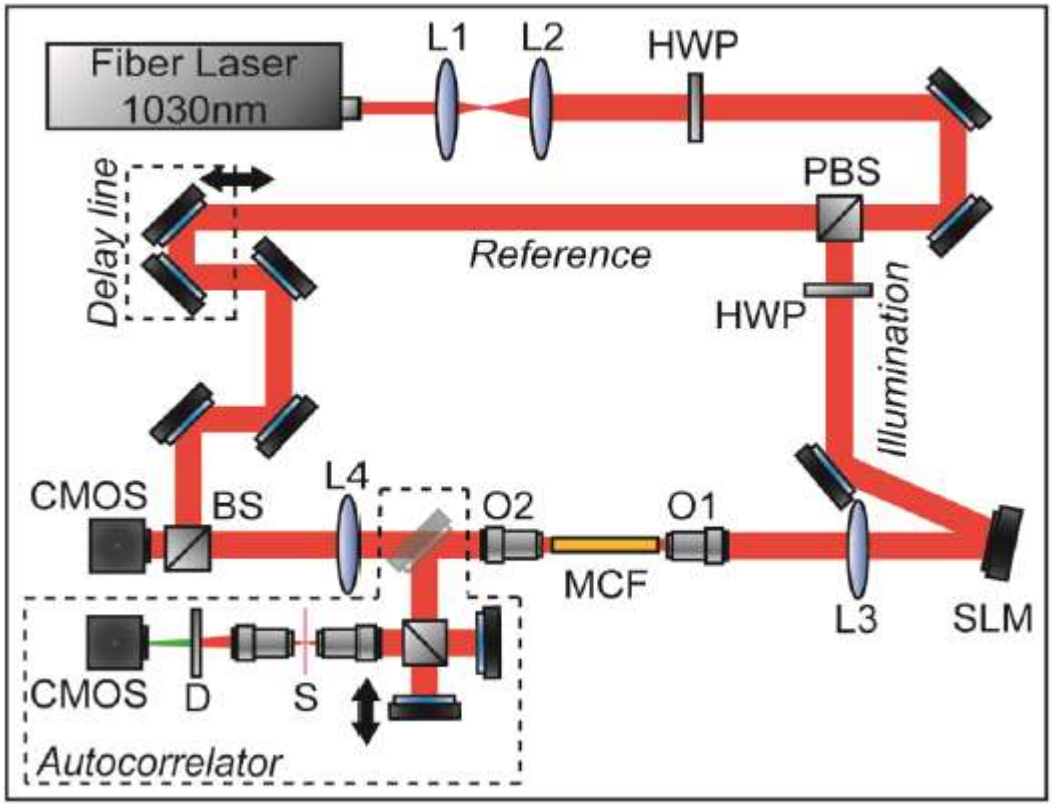

Figure 58: The optical setup for measuring the transmission matrix through the MCF. A collimated, pulsed beam is split into illumination and reference arms. The illumination path images an SLM onto the facet of a MCF. The light transmitted through the MCF is imaged onto a CMOS detector. The reference arm interferes with the illumination arm on the detector to make an off-axis digital hologram. A delay line in the reference path allows for tuning the temporal delay of the reference pulses. An interferometric auto correlator is built into the system for pulse length measurement.

***MCF:** Multi-core fiber.**HWP:** halfwave plate. **PBS:** Polarized beam splitter. **BS:** Beam splitter.*
***SLM :** Spatial Light Modulator. **D:** Dichronic filter. **S:** Sample. **L:** Lens. **O:** objective.*

Above image courtesy of Donald B. Conkey, Eirini Kakkava, Thomas Lanvin, Damien Loterie, Nicolino Stasio, Edgar Morales-Delgado, Christophie Moser, Demetri Psaltis. „High power, ultrashot pulse control through a multi-core fiber for ablation“ (2017)

More related publications:

3 Fabrication of oil-water separation copper filter by spatial light modulated femtosecond laser
Xiaoyan Sun, Zhuolin Dong, Kaifan Cheng, Dongkai Chu, Dejian Kong, Youwang Hu, JianDuan
Journal of Micromechanics and Microengineering, 30, 2020
https://doi.org/10.1088/1361-6436/ab870d

4 Amplitude-phase optimized long depth of focus femtosecond axilens beam for single-exposure fabrication of high-aspect-ratio microstructures
Deng Pan, Bing Xu, Shunli Liu, Jiawen Li, Yanlei Hu, Dong Wu, Jiaru Chu
Optics Letters, Vol. 45, No. 9, 2020, https://doi.org/10.1364/OL.389946

5 Laser surface structuring of diamond with ultrashort Bessel beams
Sanjeev Kumar, Shane M. Eaton, Monica Bollani, Belen Sotillo, Andrea Chiappini, Maurizio Ferrari, Roberta Ramponi, Paolo Di Trapani, Ottavia Jedrkiewicz
Scientific Reports, 2018, DOI: 10.1038/s41598-018-32415-0

6 High efficiency fabrication of complex microtube arrays by scanning focused femtosecond laser Bessel beam for trapping-releasing biological cells
Liang Yang, Shengyun Ji, Kenan Xie, Wenqiang Du, Bingjie Liu, Yanlei Hu, Jiawen Li, Gang Zhao, Dong Wu, Wenhao Huang, Suling Liu, Hongyuan Jiang, and Jiaru Chu
Optics Express, Vol. 25, Issue 7, https://doi.org/10.1364/OE.25.008144

7 Application of cooled spatial light modulator for high power nanosecond laser micromachining
Beck, Rainer J ,Jonathan P Parry, William N MacPherson, Andrew Waddie, Nick J Weston, Jonathan D Shephard, Duncan P Hand
Optics Express, Vol. 18, Issue 16, 2010, https://doi.org/10.1364/OE.18.017059

3.8 Wavelength Selective Switching and Telecommunication

In commercial telecommunication system the primary application of LCOS is inside WSS that enable reconfiguration and routing within optical networks by addressing different prism/blazed grating functions.

Advantage compared to conventional WSS is higher reliability and life time due to the absence of moving parts/gratings.

Industry applications: Telecommunication

3.8.1 Publications and References

1 Compact Wavelength Selective Switch Based on High-density Bragg Reflector Waveguide Array with 120 Output Ports

Xiaodong Gu and Fumio Koyama
Optical Fiber Communication Conference OSA Technical Digest (online) (Optical Society of America, 2014), paper Th3F.1, https://doi.org/10.1364/OFC.2014.Th3F.1

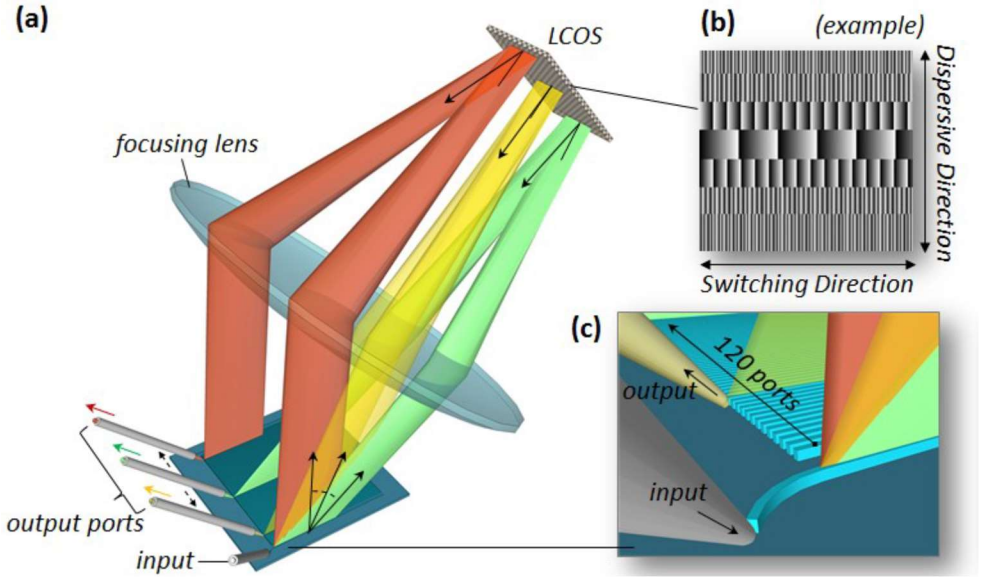

Figure 59: (a) 3D schematic view of the proposed Wavelength Selective Switch. (b) Example pattern on an Liquid Crystal on Silicon display for 7-channel operation (c) Configuration of the input waveguide and arrayed waveguides

Above image courtesy of Xiaodong Gu and Fumio Koyama. „Compact Wavelength Selective Switch Based on High-density Bragg Reflector Waveguide Array with 120 Output Ports“ (2014)

2 Beyond the display: phase-only liquid crystal on Silicon devices and their applications in photonics

Grigory Lazarev, Po-Ju Chen, Johannes Strauss, Nicolas Fontaine, and Andrew Forbes
Optics Express Vol. 27, Issue 11, pp. 16206-16249 (2019),
https://doi.org/10.1364/OE.27.016206

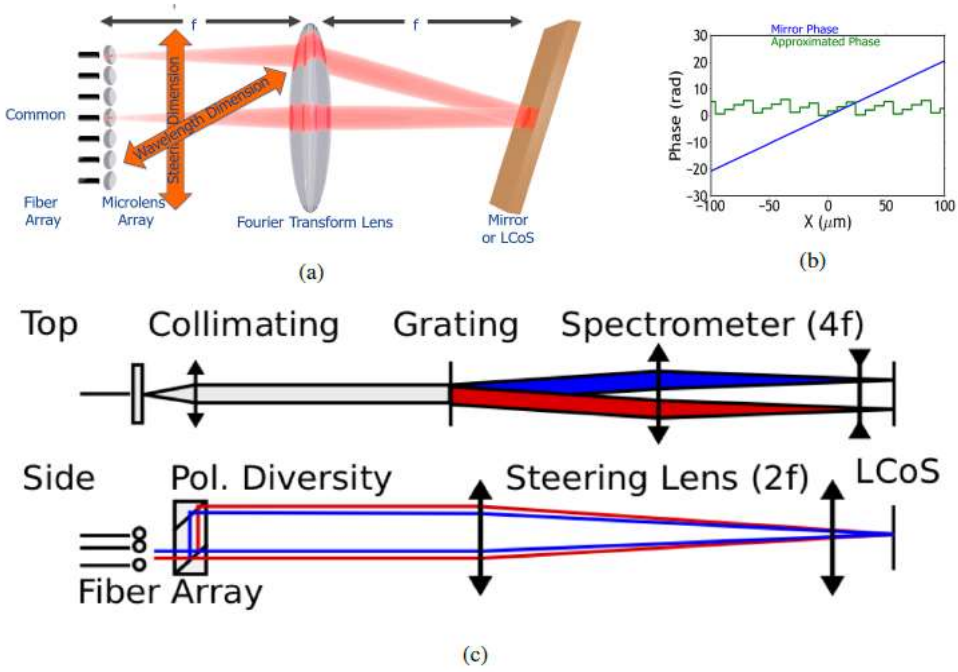

Figure 60: Principles of WSS with LCOS device:

(a) Beam steering spatial switch
(b) Mirror phase vs approximation of linear phase by Liquid Crystal on Silicon
(c) WSS with astigmatic optics for independent optimization of steering dimension and wavelength dimension including polarization optics and spectrometer section

Above image courtesy of Grigory Lazarev, Po-Ju Chen, Johannes Strauss, Nicolas Fontaine and Andrew Forbes. „Beyond the display: phase-only liquid crystal on Silicon devices and their applications in photonics“ (2019)

3 Laguerre-Gaussian mode sorter

Nicolas K. Fontaine, Roland Ryf, Haoshuo Chen, David T. Neilson, Kwangwoong Kim, Joel Carpenter
Nature Communications 10, Article number: 1865 (2019)
https://doi.org/10.1038/s41467-019-09840-4

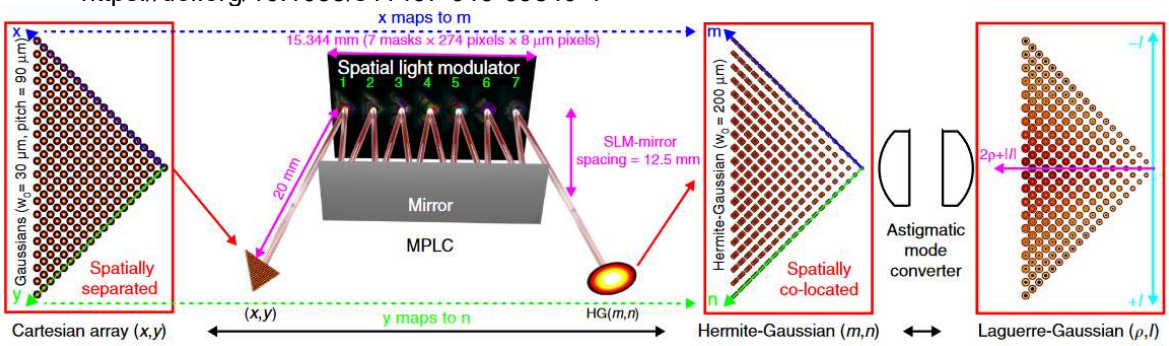

Figure 61: Laguerre-Gaussian mode sorter based on multi-plane light conversion. Cartesian grid of Gaussian spots (MFD = 60µm) at position (x,y) pass through the MPLC system, consisting of 7 phase plates separated by 25 mm of free-space propagation, implemented using a spatial light modulator and a mirror. Through these 7 planes each input spot at position x,y is mapped to a corresponding Hermite-Gaussian mode (m,n) (MFD = 400 µm), which is in turn transformed into the Laguerre-Gaussian basis through use of two cylindrical lenses.

Above image courtesy of Nicolas K. Fontaine, Roland Ryf, Haoshuo Chen, David T. Neilson, Kwangwoong Kim, Joel Carpenter. „ Laguerre-Gaussian mode sorter “ (2019)

More related publications:

4 High-Resolution Tunable Filter With Flexible Bandwidth and Power Attenuation Based on an LCoS Processor

Yunshu Gao and Genxiang Chen and Xiao Chen and Qian Zhang and Qiao Chen and Ce Zhang and Kai Tian and Zhongwei Tan and Chao Yu
Photonics Journal, 2018, DOI: 10.1109/jphot.2018.2876347

5 Measurements in two bases are sufficient for certifying high-dimensional entanglement

Jessica Bavaresco, Natalia Herrera Valencia, Claude Klöckl, Matej Pivoluska, Paul Erker, Nicolai Friis ,Mehul Malik, Marcus Huber
Nature Physics, 2018, DOI: 10.1038/s41567-018-0203-z

3.9 Mask-less and holography lithography

Photomasks for new integrated circuits with next generation design rules are increasingly more complex and costly, especially for development, prototyping, and eventual low volume production.

Optical mask-less lithography is an alternative method in which the conventional photomask is replaced by a programmable SLM that is used as an amplitude mask that will be projected on e.g. a photosensitive film.

Industry applications: Photo semiconductor device development, Micro ID numbering, MEMS, Bio-Life science complex chemistry, optical communication, projection in automotive lighting.

3.9.1 Publications and References

1 Method for single-shot fabrication of chiral woodpile photonic structures using phase-controlled interference lithography

Swagato Sarkar, Krishnendu Samanta, and Joby Joseph
Optics Express Vol. 28, Issue 3, pp. 4347-4361 (2020), https://doi.org/10.1364/OE.384987

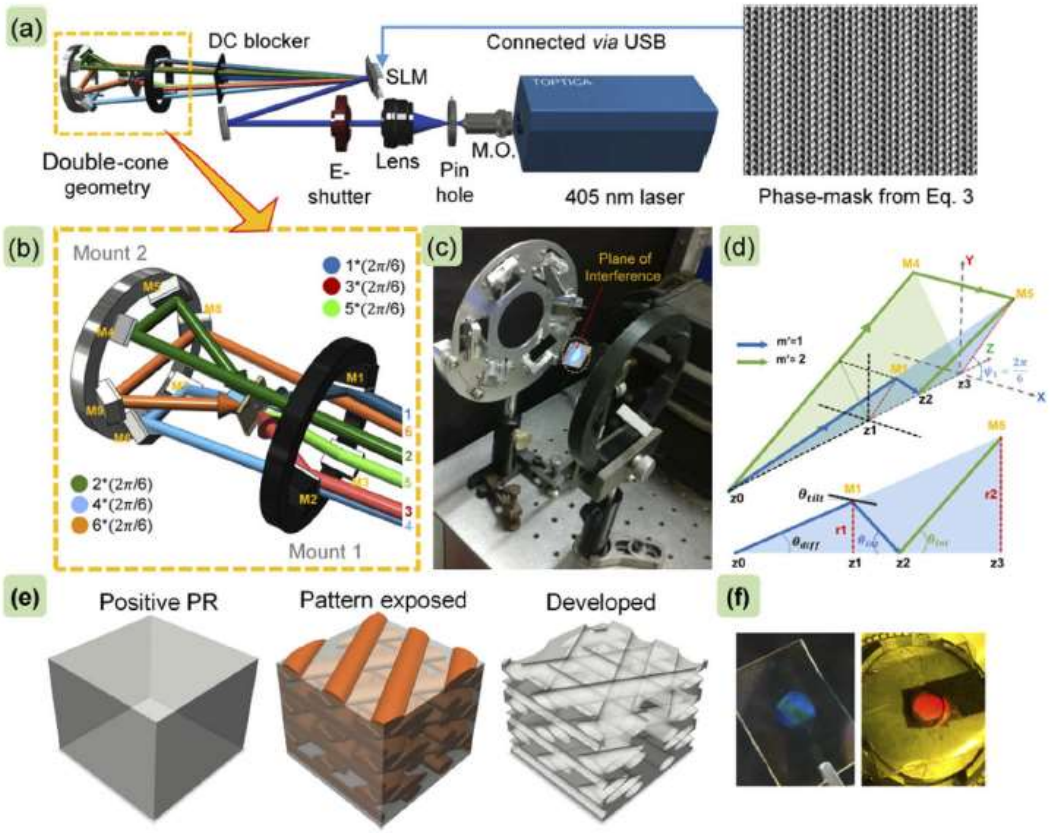

Figure 62:
(a) Experimental setup towards the realization of a chiral woodpile structure involving a dual-cone geometry. The beams diffracted in umbrella geometry from the SLM (provided with computed phase-mask) are represented with pseudo colours, each colour represents a particular phase associated with the individual beams.
(b) A magnified version of arrangement to convert six diffracted beams into 3+3 dual cone geometry using mount 1 and 2.
(c) Actual experimental counterpart of (b) with the irradiated plane of interference.
(d) Interference angle in terms of distance along the Z-axis in dual cone geometry considering beams 1 and 2.
(e) Pattern recording process in positive photoresist showing the complementary structure after development.
(f) Fabricated positive photoresist sample with complementary chiral structure showing different diffracted colours in different observing directions.

Above image courtesy of Swagato Sarkar, Krishnendu Samanta and Joby Joseph. „Method fir single-shot fabrication of chiral woodpile photonic structures using phase-controlled interference lithography“ (2020)

2 Ultrafast laser processing of materials: from science to industry

Mangirdas Malinauskas, Albertas Žukauskas, Satoshi Hasegawa, Yoshio Hayasaki, Vygantas Mizeikis, Ričardas Buividas & Saulius Juodkazis
Light Sci Appl 5, e16133 (2016), https://doi.org/10.1038/lsa.2016.133

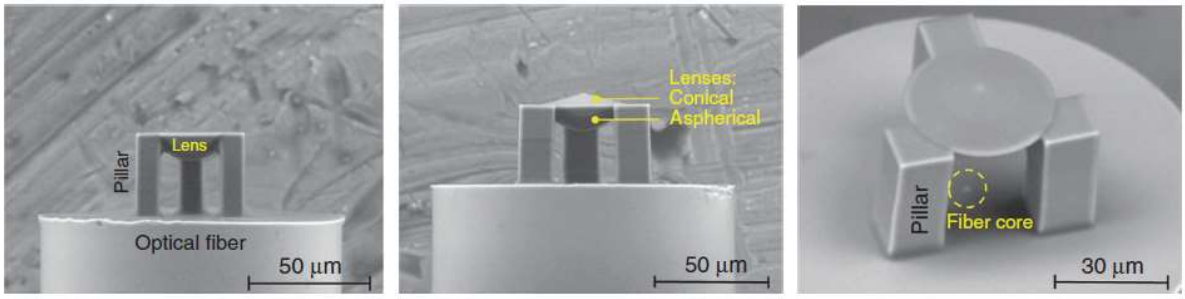

Figure 63: Freeform 3D micro optical elements fabricated by Direct Laser Writing: hybrid optical elements: aspheric and axicon lenses on a tip of optical fibre.

Above image courtesy of Mangirdas Malinauskas, Albertas Zukausks, Satoshi Hasegawa, Yoshio Hayasaki, Vygantas Mizeikis, Ricardas Buividas and Saulius Juodkazis. „Ultrafast laser processing of materials: from science to industry“ (2016)

3 Holographic Mastering System Kinemax

Polish Holographic Systems. www.kinemax.pl

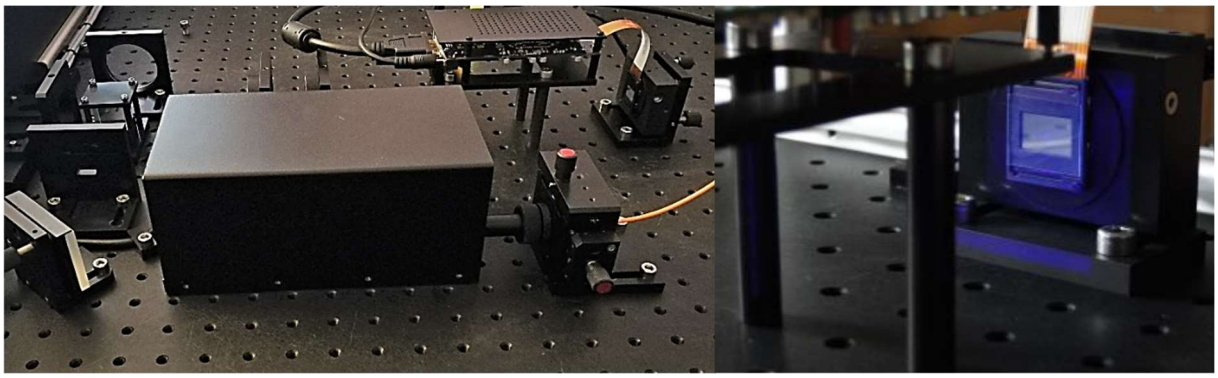

Figure 64: Optical setup of Holographic Mastering System Kinemax. Images are created with micro display and then exposed in photoresist plate. Such system has an application in: Security Holography Features, Intelligent Diffusers for Photovoltaic Panels and Mobile Displays, Maskless lithography.

Above images courtesy of Polish Holographic Systems. www.kinemax.pl

4 Maskless lithography

Rajesh Menon, AmilPatel, DarioGil, Henry I.Smith
Materials Today, Volume 8, Issue 2, February 2005, Pages 26-33,
https://doi.org/10.1016/S1369-7021(05)00699-1

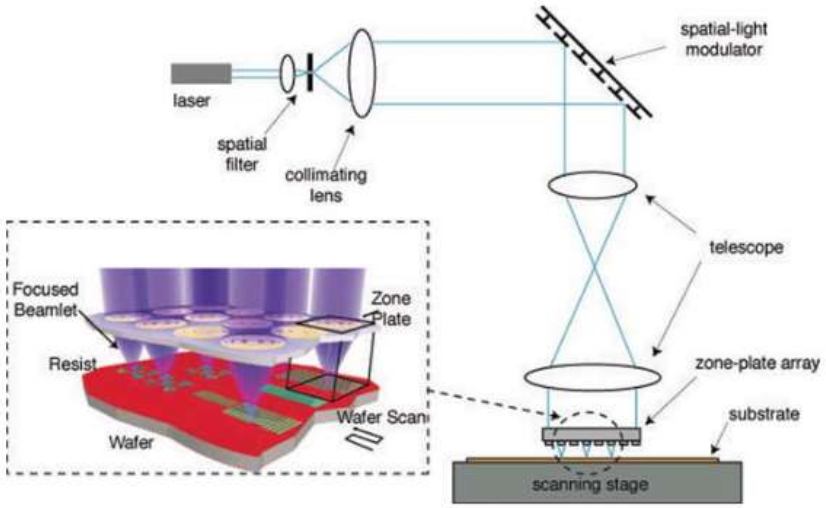

The use of an LCD SLM for microstructure pattern projection on the sample, e.g. photoresist, allows not only the realization of binary level structures but also of multilevel structures in contrast to the Digital Mirror Devices.

Figure 65: Schematic of Zone-Plate-Array Lithography. An array of zone plates (diffractive micro-lenses) focuses normally incident light into an array of spots on the surface of the substrate. Light intensity in each spot is independently controlled by pixels on an upstream SLM. The substrate is scanned and patterns of arbitrary geometry are written in a "dot-matrix" fashion.

Above image courtesy of Dario Gil. "Maskless lithography"(2005)

5 Maskless lithography for versatile and low cost fabrication of polymer based micro optical structures

Muhammad Shaukat Khan, Roland Iachmayer, and Bernhard Roth
OSA Continuum Vol. 3, Issue 10, pp. 2808-2816 (2020),
https://doi.org/10.1364/OSAC.400056

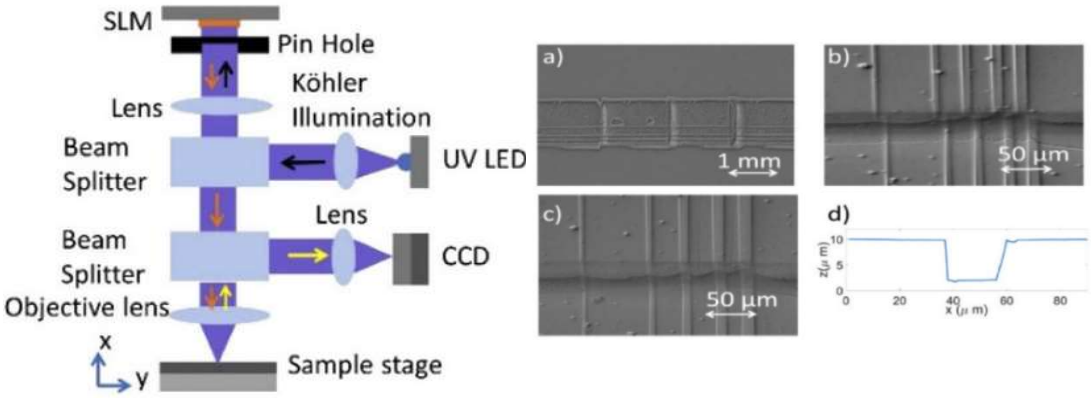

Figure 66: (Left) Maskless optical setup. In order to fabricate the desired structures, an LCD SLM is employed to modulate the incoming light in the desired shape and project it onto the sample. The modulated incoming light from the SLM is demagnified through a plan-achromatic objective lens with a numerical aperture of 0.3 and a magnification of 10. A homogenous intensity distribution of the incoming light is necessary to illuminate the SLM screen for homogenous microstructure pattern on the sample.
(Right) Fabricated stitched waveguides (a) Stitching single patterns together forming long waveguide (b) stitched patterns showing large stitching errors (c) stitched patterns with minimal stitching error (d) depth profile of the replicated waveguide structures measured with confocal microscopy.

Above images courtesy of Muhammad Shaukat Khan, Roland Iachmayer and Bernhard Roth. "Maskless lithography for versatile and low cost fabrication of polymer based micro optical structures" (2020)

More related publications:

6 Method for single-shot fabrication of chiral woodpile photonic structures using phase-controlled interference lithography
Swagato Sarkar and Krishnendu Samanta and Joby Joseph
Optics Express, 2020, https://doi.org/10.1364/oe.384987

7 Simultaneous direct holographic fabrication of photonic cavity and graded photonic lattice with dual periodicity, dual basis and dual symmetry
D. Lowell, J. Lutkenhaus, D. George, U. Philipose, B. Chen, Y. Lin
Optics Express, 2017, https://doi.org/10.1364/OE.25.014444

8 Ultrafast laser processing of materials: from science to industry
Malinauskas, Mangirdas and Zukauskas, Albertas and Hasegawa, Satoshi and Hayasaki, Yoshio and Mizeikis, Vygantas and Buividas, Ricardas and Juodkazis, Saulius
Light: Science & Applications, 2016, http://dx.doi.org/10.1038/lsa.2016.133

3.10 Polarization Generation

In recent years Spatial Light Modulators were used to produce spatially variant states of polarization controlled by computer. Different method can be used to create polarization pattern with Liquid Crystal on Silicon Spatial Light Modulator.

Due to the birefringent nature of LC based SLMs it is possible to generate any possible state of polarisation by retarding the orthogonal polarisation components against each other. Conventional LCoS displays for projection applications require a max polarisation rotation of 90° what equals a lambda/2 phase retardation.

Using a 2pi phase only SLM in combination with a quarter wave plate leads to a higher flexibility in polarisation generation to generate e.g. radially or azimuthal polarised light fields.

Industry applications: High-resolution imaging, confocal microscopy, two-photon microscopy, second-harmonic generation microscopy, dark filed imagining, microellipsometry, optical communication

3.10.1 Publications and References

1 Generation of arbitrary cylindrical vector beams on the higher order Poincare sphere

Shizen Chen, Xinxing Zhou, Yachao Liu, Xiaohui Ling, Hailu Luo, Shuangchun Wen
Optical Society of America, 260.2110 Electromagnetic optics, 260.5430 Polarization
https://doi.org/10.1364/OL.39.005274

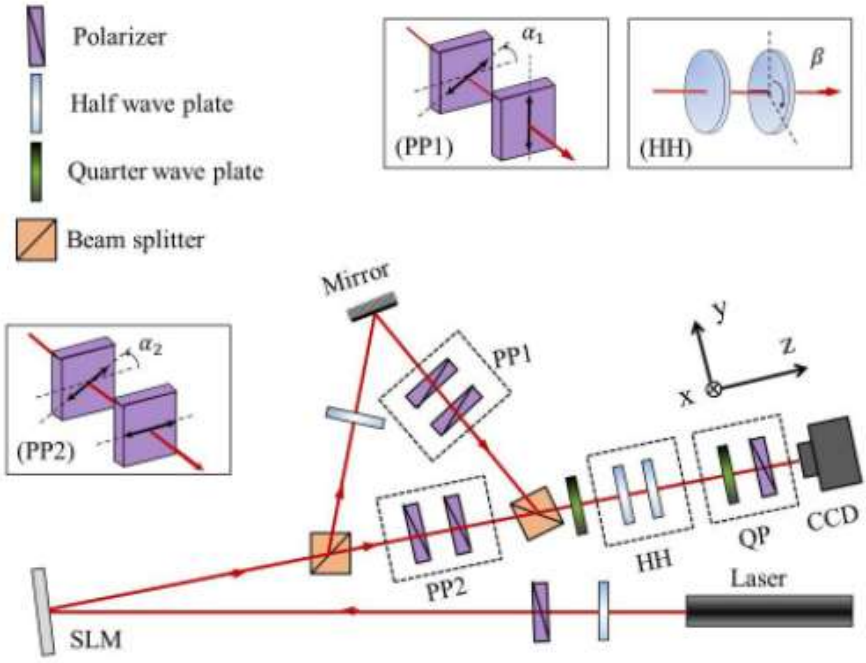

Figure 67: Experimental setup: Gaussian beam generated by a He-Ne laser passes through a HWP a Glan laser polarizer (GLP) to product a horizontally polarized beam. Then the fundamental Gaussian beam is transformed into a vortex-bearing LG^{1}_{0} mode by a spatial light modulator. The modified Mach-Zender interferometer comprising of two cascaded beam splitter and an odd number of reflections can convert the LG^{1}_{0} into LG^{-1}_{0} mode. In addition, we add PP1 and PP2 (two cascaded GLPs of which the second one is fixed) in each arm of the interferometer to justify the intensity factors. HH (a pair of of HWPs within which only the second once can be rotated) is added to modify the phase factors. QP consisting of QWP and GLP, is used to measure Stokes parameters. The intensity distribution of the field is detected by a CCD camera.

Above image courtesy of Shizen Chen, Xinxing Zhou, Yachao Liu, Xiaohui Ling, Hailu Luo, Shuangchun Wen „ Generation of arbitrary cylindrical vector beams on the higher order Poincare sphere “ (2014)

2 Cylindrical vector beams: from mathematical concepts to applications

Qiwen Zhan
Advances in Optics and Photonics Vol. 1, Issue 1, pp. 1-57 (2009),
https://doi.org/10.1364/AOP.1.000001

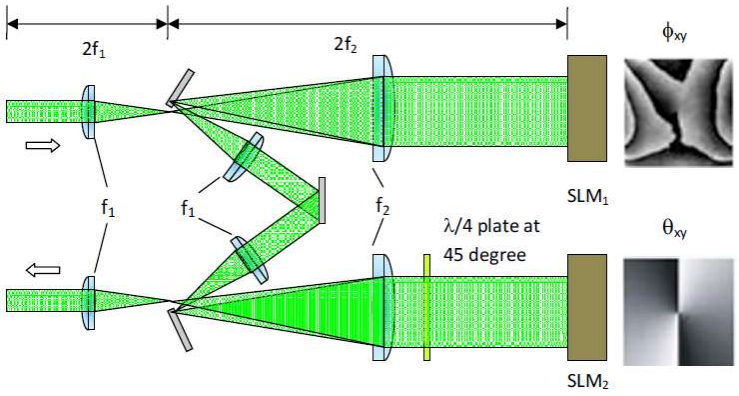

Figure 68: A polarization mode converter setup with two SLMs. The first SLM creates the desired phase pattern. The combination of the λ/4 plate and the second reflection type SLM converts the beam into the spatially variant polarization pattern. The second SLM cab be programed to convert a linear polarized beam into CV beam.

Above image courtesy of Qiwen Zhan „Cylindrical vector beams: from mathematical concepts to applications“ (2008)

3 Compact LCOS–SLM Based Polarization Pattern Beam Generator

Xuejie Zheng, Angel Lizana, Alba Peinado, Claudio Ramírez, Jose L. Martínez, Andrés Márquez, Ignacio Moreno, and Juan Campos
Journal of Lightwave Technology Vol. 33, Issue 10, pp. 2047-2055 (2015)

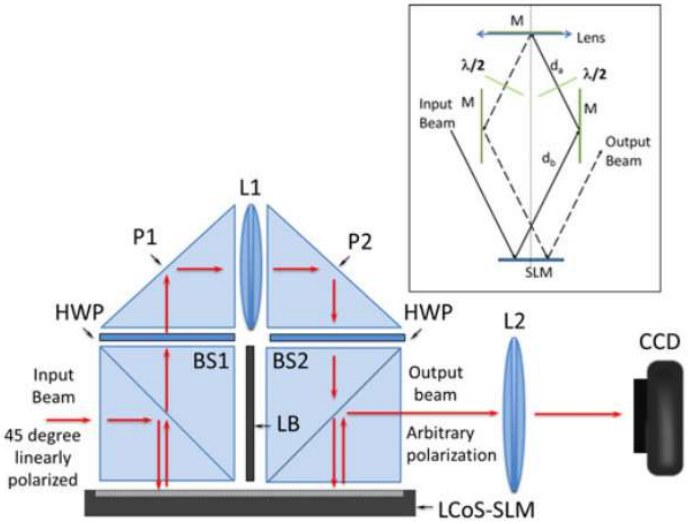

Figure 69: Scheme of the optical setup where Liquid Crystal on Silicon Spatial Light Modulator indicates the display. HWP1 and HWP2 indicate half-wave plates with 22.5 ° relative angles. BS1 and BS2 are non-polarizing beam splitters. L is a converging lens. LB indicates a light barrier to block light. Red arrows indicate the trajectory of the modulated beam. Inset: Alternative set-up without the use of beam splitters, based on the combination of three mirrors and one lens.

Above image courtesy of Xuejie Zheng, Angel Lizana, Alba Peinado, Claudio Ramirez, Jose L. Martinez, Andres Marquez, Ignacio Moreno and Juan Campos. „Compact LCOS-SLM Based Polarization Pattern Beam Generator“ (2015)

4 Digital Stokes polarimetry and its application to structured light: tutorial

Keshaan Singh, Najmeh Tabebordbar, Andrew Forbes, and Angela Dudley
Journal of the Optical Society of America A Vol. 37, Issue 11, pp. C33-C44 (2020), https://doi.org/10.1364/JOSAA.397912

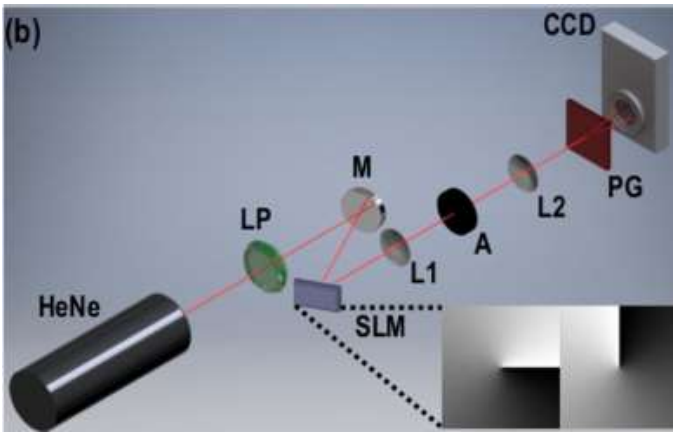

Figure 70: Experimental diagram illustrating the arrangement of the optical components used to acquire Stokes parameters for a LCoS-SLM. The representative holograms encoded onto SLM are provided as inset.

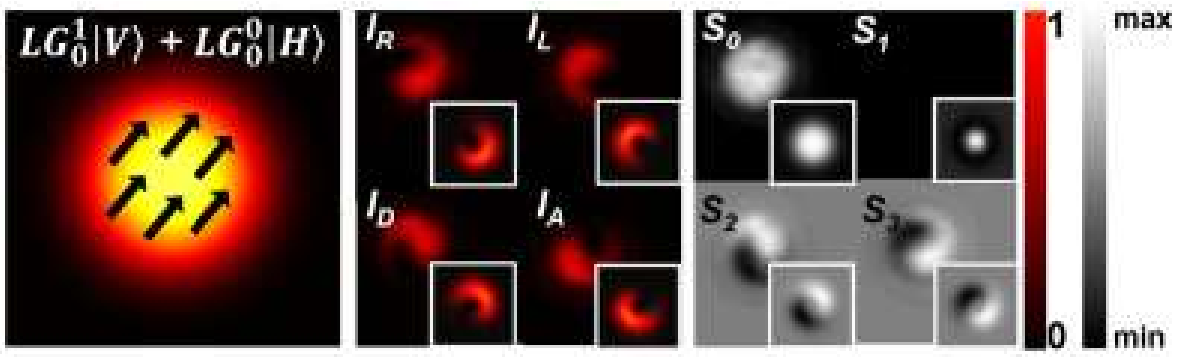

Figure 71: Digital LCoS-SLM Stokes polarimetry. From left: 1. The generated field of interest, on which the Stokes polarimetry is performed. 2. Measured intensity profiles of the Stokes projections. 3. The corresponding calculated Stokes parameters. Theoretical simulations are given as insets.

Above images courtesy of Keshaan Singh, Najmeh Tabebordbar, Andrew Forbes and Angela Dudley. „Digital Stokes polarimetry and its application to structured light: tutorial“ (2020)

If you have any further questions, please get in contact with HOLOEYE:

HOLOEYE Photonics AG
Volmerstr. 1
12489 Berlin
slm@holoeye.com
www.holoeye.com